ORIGINAL PAPER

Extreme storm surges and waves and vulnerability of coastal bridges in New York City metropolitan region: an assessment based on Hurricane Sandy

K. Qu[1,2] · W. Yao[3] · H. S. Tang[2] · A. Agrawal[2] · G. Shields[4] · S. I. Chien[5] · S. Gurung[2] · Y. Imam[6] · I. Chiodi[7]

Abstract

Hurricane Sandy struck the New York metropolitan area in October 2012, becoming the second-costliest cyclone in the nation since 1900, and it serves as a valuable basis for investigating future extreme hurricane events in the area. This paper presents a hindcast study of storm surges and waves along the coast of the Mid-Atlantic Bight region during Hurricane Sandy using the FVCOM-SWAVE system, and its simulation results match observed data at a number of stations along the coastline. Then, as potential future scenarios, surges and waves in this region are predicted in synthetic hurricanes based on Hurricane Sandy's parameters in association with sea-level rise in 50 and 100 years as well as with eight paths perturbed from that of Sandy. The prediction indicates that such surges and waves exhibit complex behaviors, and they can be much stronger than those during Hurricane Sandy. Finally, an assessment of hydraulic vulnerability is made for all coastal bridges in the New Jersey and New York region. It shows that hydrodynamic load and scour depth at some bridges may be worse in certain scenarios than those during Superstorm Sandy, while the probability of structural failure is small for the majority of them.

Keywords Storm surge and wave · Hurricane Sandy · Sea-level rise · Hurricane path · Coastal bridge · Hydraulic vulnerability

✉ H. S. Tang
htang@ccny.cuny.edu

1   School of Hydraulic Engineering, Changsha University of Science and Technology, Changsha 410114, China

2   Department of Civil Engineering, City College of New York, CUNY, 138th Street and Convent Avenue, New York, NY 10031, USA

3   Boston Consulting Group, New York, NY 10001, USA

4   Department of Construction Management and Civil Engineering Technology, New York City College of Technology, CUNY, Brooklyn, NY 11201, USA

5   Department of Civil and Environmental Engineering, New Jersey Institute of Technology, Newark, NJ 07102, USA

6   North Cross School, Roanoke, VA 24018, USA

7   Friends Seminary, New York, NY 10003, USA

1 Introduction

Historically, many storms have led to extreme ocean surges and waves, and they have caused a catastrophic loss in the New York City (NYC) metropolitan region. Landing with an enormous size in the region at the end of October 2012, Hurricane Sandy drove record storm surges and led to over $100 billion in damage to the New York (NY) and New Jersey (NJ) area and more than 147 deaths in the Northeast USA, Canada, and the Caribbean (CNNlibrary 2016). As a result, Hurricane Sandy became the second-costliest cyclone, behind Hurricane Katrina in 2005, to hit the USA since 1900 (Torres et al. 2015). Overall, Hurricane Sandy had a widespread impact on the region, including the seabed (Hu et al. 2018), structural systems (Hatzikyriakou and Lin 2017), ecosystems (Hallett et al. 2018), and public health (Shultz et al. 2019). Therefore, in many ways, Hurricane Sandy serves as a call to action to investigate potential extreme surges and waves and their potential impact in the NYC metropolitan region during future hurricanes. The necessity for such action is further manifested by: (a) the rate of sea-level rise (SLR) in the Northeast USA that is estimated to be twice the global average value and (b) the increase in the frequency of strong hurricanes in the region (Vecchi and Knutson 2008; Yin et al. 2009).

During the past few years, various methods were applied to simulate ocean surges and waves as well as the consequent coastal flooding in the NYC metropolitan region. For instance, Lin et al. (2010) assessed storm surges in the NYC coastal region using many synthetic surge events. Tang et al. (2013b) predicted high-resolution coastal flooding in the eastern bank of Delaware Bay in SLR conditions through a coupled modeling system. Blumberg et al. (2015) presented a high-resolution simulation to study flooding in the streets near the bank of the Hudson River during surge inundation. Orton et al. (2016) carried out a prediction based on past events to understand flooding hazards in New York Harbor. Miles et al. (2017) made a numerical investigation combined with field observation on ocean currents along NY and NJ coastlines during Sandy. Bennett et al. (2018) conducted a modeling study to examine water-level variability in Great South Bay, New York, during Hurricane Sandy.

Efforts have also been made during recent years on the hydraulic vulnerability of environments, ecosystems, infrastructure, and others components of our physical infrastructure to storm surges and waves in the NYC metropolitan region. Tang et al. (2013a) predicted the vulnerability of residential communities and transportation systems to coastal flooding near the eastern bank of the Delaware Bay following sea-level rise conditions. Kress et al. (2016) simulated storm surges during Hurricane Sandy and have examined the effectiveness of flood mitigation structures. Meixler (2017) quantified the impact of Sandy on sediment deposition and marsh habitat in Jamaica Bay, NY, and made recommendations for its restoration. Hatzikyriakou and Lin (2017) developed fragility curves to correlate building damage during Hurricane Sandy with the significant wave height. Regarding damage to ecosystems and public health due to flooding during hurricanes, Hallett et al. (2018) reported that a substantial number of trees flooded by saltwater in inundation zones in NYC during Sandy failed to leaf out in the following year. Malik et al. (2018) found that older adults were more vulnerable to adverse health effects of the hurricane event. Markogiannaki (2019) presented a procedure of risk assessment for cable-stayed bridges during earthquakes and hurricanes in the NYC. It is noted that numerous studies were made for other regions. For instance, Kantamaneni (2016) presented an index of vulnerability to quantify coastal flooding, surges, and erosion in Wales. Apollonio et al. (2020) simulated the inundation of different scenarios at southern Italy and estimated risk in economy loss.

In spite of the studies identified above, still there is lack of a clear understanding on extreme surges and waves during Hurricane Sandy and also those potential ones in the future, and their consequential risk to the NYC metropolitan region. Because of storms' complexity and uncertainty, past studies tended to focus on local regions and limited to areas with relatively small sizes. For instance, a hindcast was made on storm surges around on Staten Island during Hurricane Sandy based on calibration with data from a few observation stations (Kress et al. 2016). In another hindcast study of inundation during Sandy, data for validation came from observations along the southern banks of NYC, and the area of study was primarily limited to Great South Bay, New York (Bennett et al. 2018). In an assessment of future flood hazards by Orton et al. (2016), the area centered on the New York Harbor. In Hatzikyriakou and Lin (2017), the study was focused on influence to a community at Ortley Beach, NJ. While all these local investigations are necessary, it is also important that we improve our understanding on overall and regional scenarios of storm surges and waves, and the risk to the entire NYC metropolitan coastline. Besides an understanding of storm surges and waves, the vulnerability of coastal transportation infrastructure in this region has also become a significant concern following massive damage during Hurricane Sandy (Coch 2015). Transportation infrastructure, such as coastal bridges, plays a critically important role for residential and business activities in this region. While a few such investigations exist for this region, such as Jacob et al. (2011) and Tang et al. (2013a, b), more research is needed for improving our understanding.

This study aims at improving our understanding on potential future extreme surge and wave action and the corresponding vulnerability of coastal bridges in the NYC metropolitan region. Since Hurricane Sandy is one of the most catastrophic storm events in the region, it is used as the basis of this study. The study attempts to fill the aforementioned knowledge gaps, and it is novel in several fronts. In particular, first, a hindcast of storm surges and waves during Sandy was made for a large area, including coastlines of the tri-state (i.e., New Jersey, New York, and Connecticut), rather than local zones in most past work as indicated above. The simulation model was calibrated using field data of water surface elevation and wave height from a number of observation stations scattered along the tri-state coastline. Then, considering the strength of Hurricane Sandy coupled with sea-level rises and hypothetic tracks, a prediction was made for storm surges and waves in the entire region. Finally, as a novel aspect, a thorough search was conducted among all coastal bridges in NJ and NY, and analysis was performed on the basis of available engineering methods to investigate the vulnerability of those identified as the most vulnerable ones to hydrodynamic impact, sediment scour, and structural failure. It is indicated that, in this study, a multidisciplinary approach is adopted, e.g., ocean science, coastal engineering, and bridge engineering, which is relatively fresh.

2 Model setup

2.1 Region of study, model, and parameters

The computational domain covers the eastern coast of the USA, beginning in Florida and ending in Prince Edward Island, Canada, in a range from the latitude of 27.4°N to 45.8°N and the longitude of 81.5°W to 60.1°W, as shown in Fig. 1a, and the region of study focuses on the Mid-Atlantic Bight (MAB), see the enclosed zone in Fig. 1a, with zoom-in Fig. 1b–f. In the computational domain, water depth is less than 30 m in
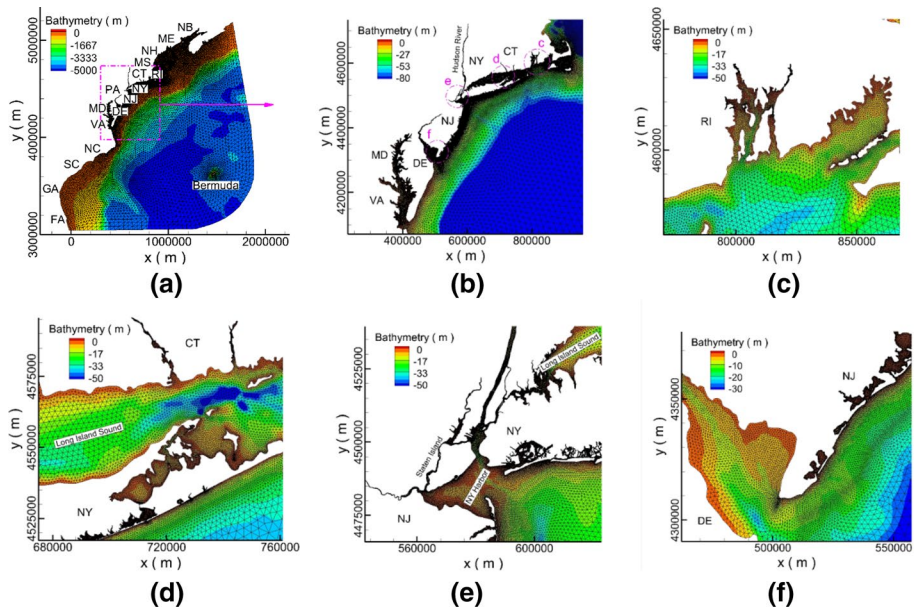
Fig. 1 Computational domain, bathymetry, and mesh

the nearshore region, and it is as deep as 5458 m in the offshore region. The bathymetry data in the shallow water region next to the coast have been obtained from the National Geophysical Data Center (NOAA NGDC 2020). In the deep-water region, it is derived from ETOPO1, which is a one arc-minute global relief model of Earth's surface that integrates land topography and ocean bathymetry (NOAA ETOPO1 2020). The NOAA bathymetry data have a resolution of approximately 100 m for a majority of the nearshore zone, and NOAA's VDATUM is used to convert the bathymetric data to the common vertical datum NAVD88 (Parker et al. 2003). The seashore boundaries are defined by the NOAA high-resolution composite vector shoreline (NOAA CSC 2020). In this study, flow boundaries are fixed, and no flooding on land is considered. In addition, at the locations where small rivers are not included in the high-resolution dataset (NOAA CSC 2020), NOAA medium-resolution coastlines are used (NOAA SCR 2020). Bathymetry and mesh, together with their zoom-in views, are shown in Fig. 1.

The coupled FVCOM-SWAVE modeling system is adopted for the simulations in this paper (Qi et al. 2009). This system uses an unstructured-grid, finite-volume method, and it is developed from the Finite Volume Coastal Ocean Model (FVCOM) by including the Simulating Wave Nearshore (SWAN) model. A triangular mesh is used in the horizontal plane (Fig. 1), and 11 σ-layer mesh is adopted in the vertical direction. Horizontally, its resolution varies from ~200 m in the coastal region to ~46 km in the open ocean, and triangular elements with ~10 m in size are used to resolve tributaries along the coastlines. The mesh consists of 166,294 nodes and 291,665 elements in the horizontal plane, plus 11 σ-layers in the vertical direction. It is worth noting that the mesh's numbers for elements and nodes are not large, but it has enough resolution to resolve the local geometries, such as channels with bridges. In the computation, the external time step $t_I = 0.25$ s and ISPLIT = 10 are applied during the first 5–6 days. Then, the external time step is decreased to $t_I = 0.0625$ s for the sake of numerical stability during the rest

of the computation. Other parameters required for setting up the FVCOM-SWAVE system are summarized in Table 1.

2.2 Wind and air pressure

As external forcing, a blending of the Hurricane Research Division (HRD)'s Real-time Hurricane Wind Analysis System (*H**Wind) dataset (Powell et al. 1996, 1998, 2008, 2010) and North American Regional Reanalysis (NARR) wind dataset (NOAA NCEI 2020) is utilized as surface wind and pressure forcing for the modeling system. In this study, the H*Wind dataset is used in a square domain of 960 km×960 km, and NARR dataset is employed in the rest region, both centering at the hurricane eye. Since there is a difference between the wind fields from the two datasets, the two wind fields are blended using a linear weighting function, so there is a smooth transition between them. As a result, the wind speed of the blended wind field, V_{wind}, is represented as

$$V_{wind} = \frac{s}{210} V_{H*} + \left(1 - \frac{s}{210}\right) V_{NARR} \tag{1}$$

where V_{H*} and V_{NARR} are the speeds of *H** and NARR winds, respectively, and s represents the distance to the NARR wind region.

Additionally, to further improve the quality of the blended wind field, an adverse distance-based weighting process is implemented to treat its discrepancy from the measured wind data, and the wind is adjusted by

$$\Delta V_{wind} = \sum_i^N \frac{1/s_i^2}{\sum_i^N 1/s_i^2} \Delta V_i \tag{2}$$

where N is the total number of wind stations, ΔV_{wind} is the wind adjustment at specific locations, s_i represents the distance to the ith wind station, and ΔV_i is the peak value discrepancy from the measured wind data at ith wind station.

The blended wind field at 10 m above the sea surface has been compared with the observation data of wind speed, V_{wind}, wind direction, θ_{wind}, and air pressure, p_{wind}, at 10 wind stations in the MAB region, whose locations are shown in Fig. 2 and latitudes and longitudes are available from the NOAA's buoy center (NOAA NDBC 2020). The detailed comparison is presented in Figs. 26, 27, and 28 in "Appendix A," in which a peak, a jump/drop, and a trough all correspond to the arrival time of the hurricane. In general, the blended wind field matches the actual measured data very well, although some discrepancies are

Table 1 SWAVE parameters	Parameters	Value
	Frequency range (Hz)	0.05–0.5
	Frequency bins	24
	Direction	Full circle
	Direction bins	24
	Bottom friction	Jonswap formulation
	Friction parameter	0.067
	Minimum water depth (m)	0.05
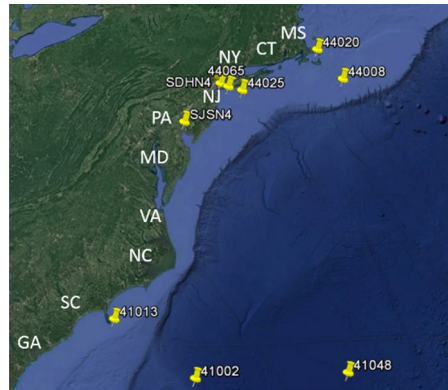
present during the hurricane. Figure 3 shows the wind field at a few instances when the hurricane travels to and away from the NYC metropolitan region.

The surface wind stress is calculated using $\tau = \rho_{air} C_d V_{wind}^2$, where ρ_{air} is air density, V_{wind} is the blended wind speed at an elevation of 10 m above the sea level, and C_d is the drag coefficient that is determined by (Sun et al. 2013)

$$
C_d = \begin{cases} 1.0 \times 10^{-3}, & 0 < V_{wind} \leq 4 \text{ m/s} \\ \left(1 + 1.5\frac{V_{wind}-4}{27-4}\right) \times 10^{-3}, & 4 \text{ m/s} < V_{wind} \leq 27 \text{ m/s} \\ 2.5 \times 10^{-3}, & V_{wind} > 27 \text{ m/s} \end{cases} \tag{3}
$$

This equation is obtained from the 10 m neutral C_d in COARE3 (Fairall et al. 2003), COARE4 (Edson 2009), and Large and Pond (1981) for $V_{wind} \leq 26$ m/s. It has been used by Sun et al. (2013) to study the storm surge and waves induced by Hurricane Bob in 1991. As reported by these authors, C_d reaches a maximum value in the range 30–35 m/s and then decreases at a higher speed.

2.3 Open boundary forcing

At the open boundary of the computational domain, water surface elevation is specified with the astronomic tide conditions provided by software OTPS, which adopts the TPXO7.2 global oceanic tidal model. The model is calibrated with measurements obtained from the TOPEX/Poseidon and Jason satellites, and it includes 13 tidal components of the water surface elevation: eight primaries (M2, S2, N2, K2, K1, O1, P1, and Q1), two long periods (Mf, Mm), and three nonlinear (M4, MS4 and MN4) constituents (Egbert et al. 1994). Since the effect of inflows from small rivers is negligible during a storm surge event, only inflows from the Delaware River and the Hudson River are considered in this study. The water surface elevations downloaded from United States Geological Survey (USGS) (USGS CWD 2017) are imposed at the two rivers. For the wave model SWAVE, a nonreflecting boundary condition is imposed at the open boundary, and zero height of wave is imposed at coastal and riverbanks as a boundary condition, absorbing all incoming wave energy.
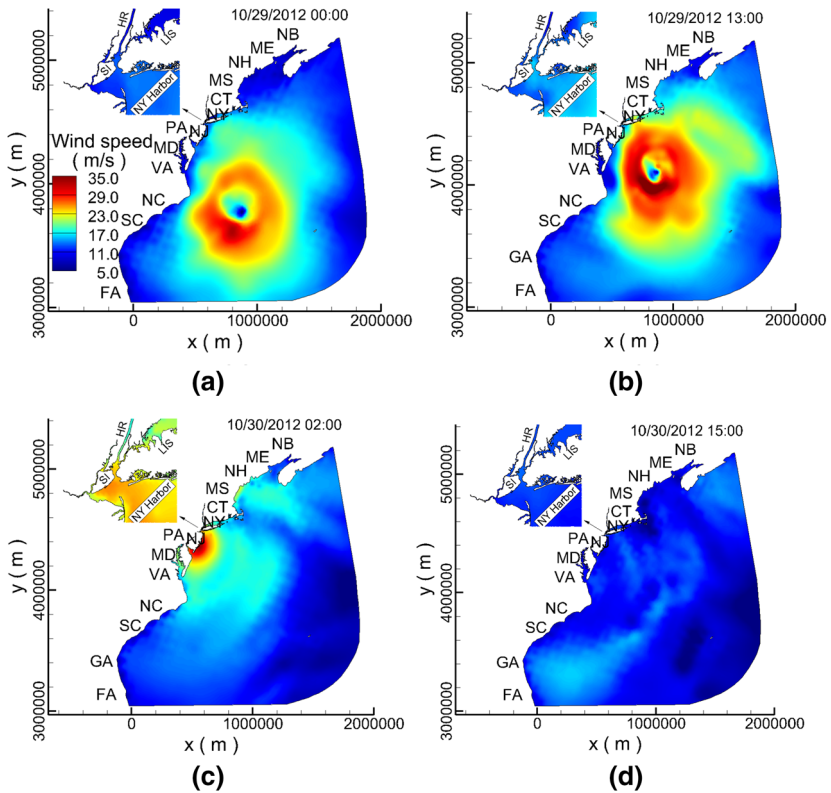
Fig. 3 Instant speed distribution of the blended wind field

3 Hindcast of storm surges and waves during Hurricane Sandy

Based on model setup and parameters discussed in previous sections, a hindcast is made for the storm surges and waves induced by the Superstorm Sandy during October 23–31, 2012. The computation of FVCOM-SWAVE is carried out on a desktop computer. Within the computational domain, there are 18 observation stations for water surface elevation and another 10 stations for wave, and many of these stations are scattered along the coastlines of NJ, NY, and CT, see Fig. 4. A comparison of the computed water surface elevation, η, with that observed at the 18 stations is presented in detail in Fig. 29 of "Appendix B." The simulated elevation is in good agreement with the observation data at most stations; not only the simulation captures the patterns of the surges, but also its values match the observed values very well at these stations. A noticeable difference between the simulation and observation occurs for certain time intervals at a few stations, and the reasons for such discrepancy are complex. For instance, the discrepancy at Station 8534720 could be attributed to the fact that the station is close to the coast and thus the flow becomes complicated, which makes it difficult to be captured by the simulation.

The simulated wave is also examined at the 10 observation stations for wave. A detailed comparison of the simulated significant wave height, H_s, and peak wave period, T_p, with the observed data is shown in Fig. 30 in "Appendix B." It is found that, in general, the simulation captures the wave's patterns in speed and period. The time when the hurricane
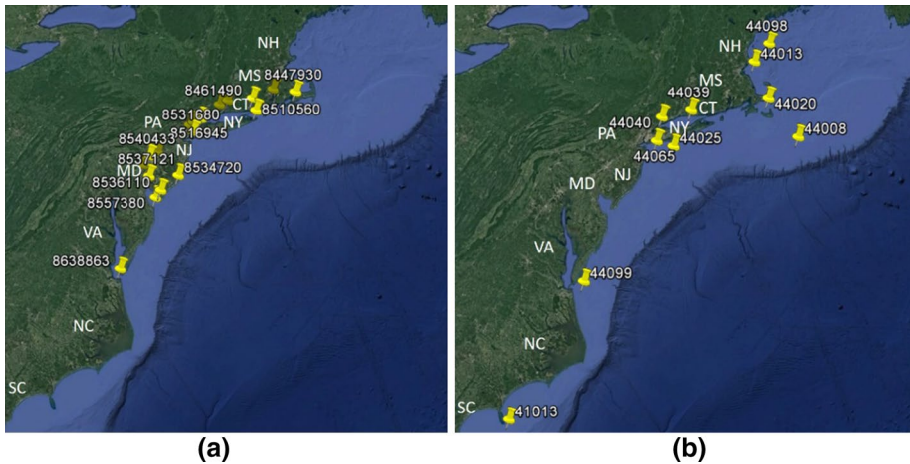
Fig. 4 Locations of observation stations. Google map. **a** Stations for surface elevation. **b** Stations for wave

hits these stations corresponds to the peak wave height, and it is captured at most of the stations by the simulation. However, there is discrepancy in simulated and observed data, especially in wave period, for which the observed data have more frequent scatter. It should be noted that the simulation of surface wave remains a challenging task, especially during hurricanes in which both current and wave fields are highly transient and local. Still, the comparison between the simulation and observation at these stations gives us a degree of confidence over the overall simulated wave field during Sandy.

As another part of the hindcast for Hurricane Sandy, a few snapshots of the simulated water surface elevations at different time instances is plotted in Fig. 5. The figure illustrates how the storm surges would evolve as the hurricane approaches, arrives, and leaves the NYC metropolitan region, whose corresponding locations can be seen in Fig. 3. It is found that water elevation would yield the maximum as the hurricane center lands this region (Figs. 3a, b and 5a, b). The increase of water surface elevation in the New York Bight, particularly at the mouth of the Hudson River and around the Staten Island (see Fig. 5c), is attributed to the convergent shape of the Bight and the counter-clockwise rotation of the hurricane. It is worth noting that the highest surface elevation in the Bight reaches as high as 3.5 m, and that along most of the NY and NJ coastlines yields 1 m approximately, which is consistent with the values reported in the literature (Bennett et al. 2018).

As shown in Fig. 6, the current velocity, U, also increases along the coast and in rivers, e.g., the Hudson River, in the NYC metropolitan region with the arrival of the hurricane. In the entire computational domain, high current speed primarily occurs in the shallow water next to shorelines, especially along the coast of NJ and DE. Additionally, a large area to the east of the Long Island Sound (LIS) undergoes high current speed for a long duration, even after the hurricane leaves the NYC metropolitan region (Figs. 3d and 6d). Along the NJ coast, the speed reaches the magnitude of mostly 1 m/s, and this is consistent with values reported in the literature (Miles et al. 2017). The simulated maximum current velocity ranges from 0.0 to 4.0 m/s in the computational domain during Hurricane Sandy, and the maximum occurs at Pelican Island, New York, USA. From a comparison of Figs. 5 and 6, it is observed that, while the change of distribution of water surface elevation is relatively
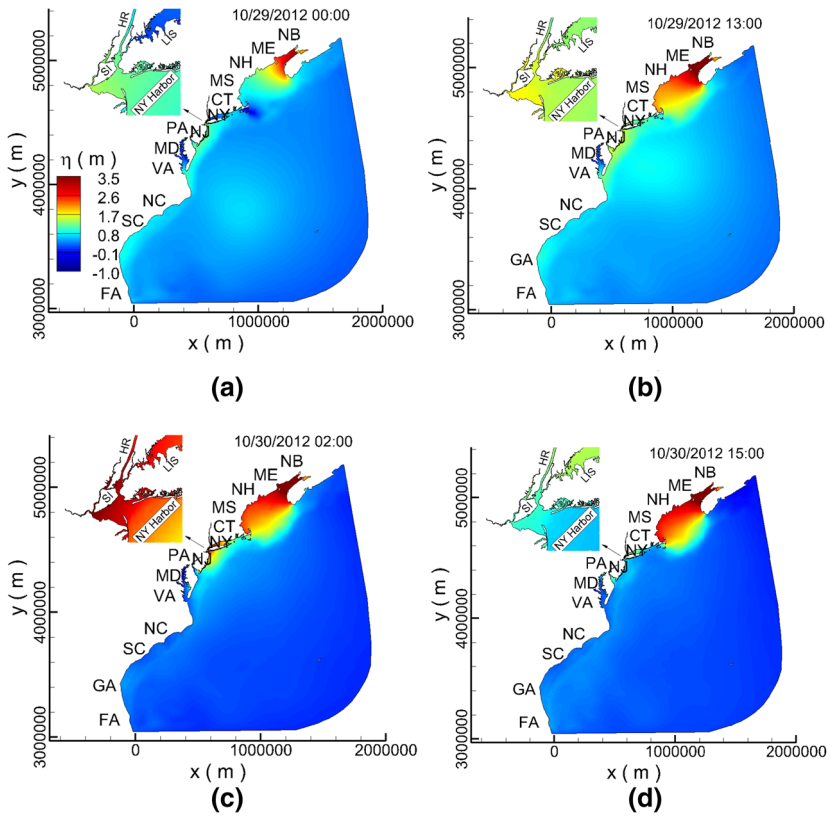
Fig. 5 Snapshots of instant water surface elevations during Hurricane Sandy

mild and gradual, velocity distribution has more locality with sudden alteration, leaving small zones with high-speed scatters.

Figure 7 shows the distribution of wave height at different time instances. It is observed that the ocean experiences high waves, as high as approximately 15 m, in large areas, primarily in the open areas of the ocean. The locations and the shapes of areas with high waves correspond to those of the wind fields of the hurricane (Fig. 3). As the Hurricane Sandy arrives, the waves become high in coastal waters of the metropolitan region. For instance, at 2 am on the October 30th (Fig. 7c) they reach approximately 8 m at the south bank of NYC, which is consistent with the literature. It was reported that the highest wave height was about 10 m in the Great South Bay next to the bank (Bennett et al. 2018). However, as seen in Fig. 7a–c, the waves in most coastal waters within a close distance to coastlines along the metropolitan NYC region, such as the New York Bight, the Hudson River, and LIS, remain at relatively low levels.
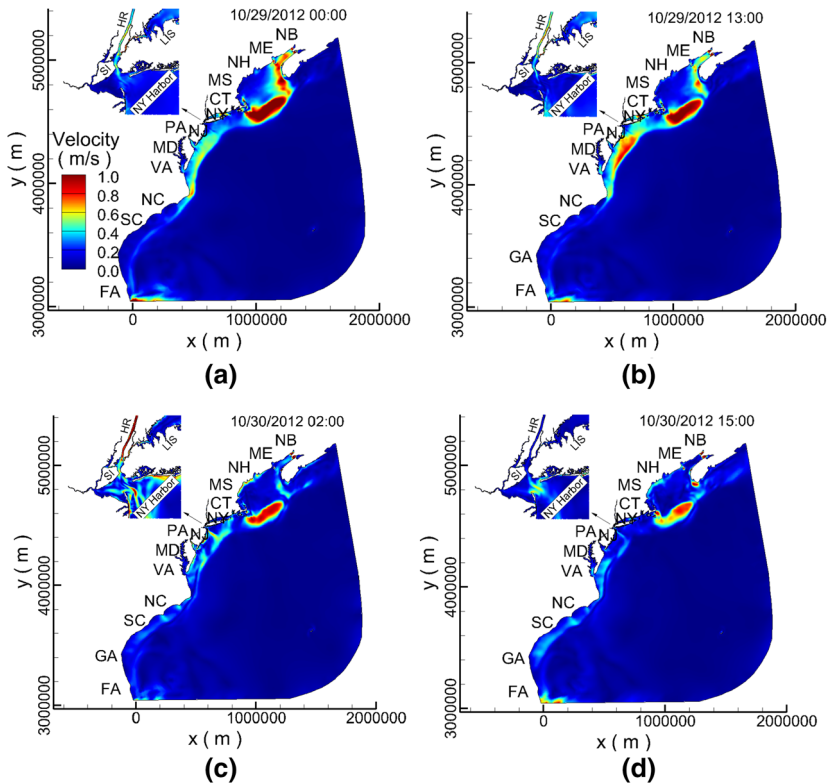
Fig. 6 Snapshots of depth-averaged current velocity distribution at different time instances during Hurricane Sandy

4 Prediction of future extreme surges and waves

4.1 Storm surge and wave in SLR condition

As shown by Tang et al. (2014a, b), SLR has an influence over water surface elevation and current speed in the MAB region when there is no storm, and it is expected that it will also have an influence on them during a future hurricane. It is projected that the median range of the global SLR over the next 100 years will be from 0.2 to 0.6 m, and it could range from 0.8 to 2 m by 2100 under the most unfavorable conditions (Solomon et al. 2007; Pfeffer et al. 2008). According to a study by Yin et al. (2009), climate change is expected to cause the sea level along the northeastern US coastlines to rise almost twice faster than the global sea level during this century. In this study, SLR scenarios of 0.5 and 1 m are considered, which roughly correspond to the estimated median values of SLR in the region of study in 50 and 100 years, respectively. The future storm is set as Hurricane Sandy; the computational settings and parameters of Sandy in Sect. 3, such as its route and wind field, are applied.

The SLR effects are examined in terms of the difference of maximum surface elevation during storms. Note that the maximum elevation is defined as the largest deviation of
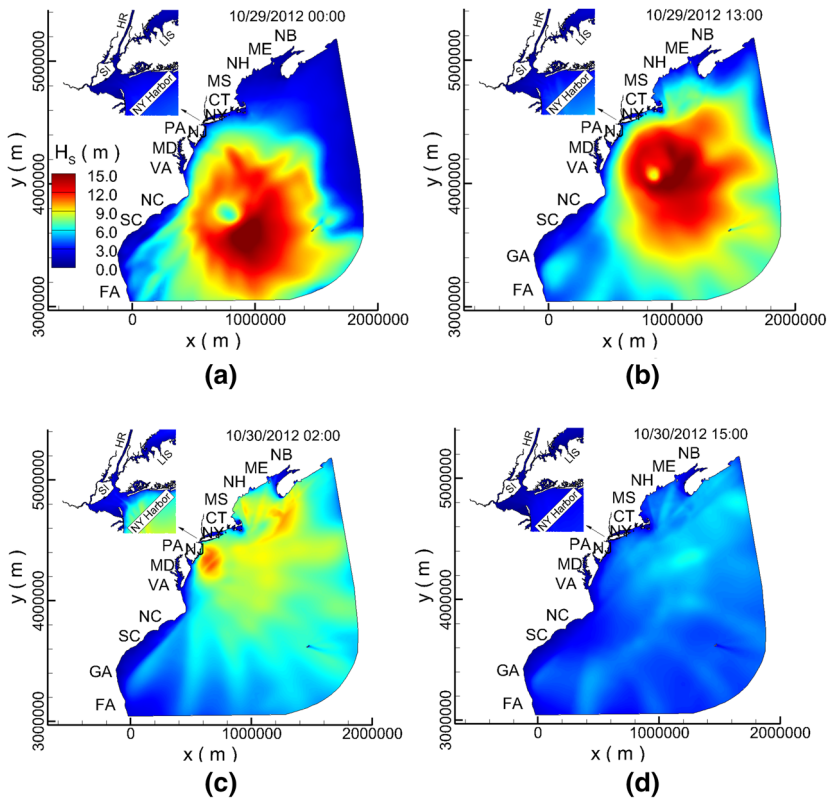
Fig. 7 Snapshots of significant wave height distribution at different time instances during Hurricane Sandy

surface height from that of without a storm. Therefore, the true difference in the maximum water surface elevation with SLR of 50 and 100 years during the future storm and that during Sandy should add 0.5 and 1 m, respectively. Figure 8 presents the difference of the maximum elevation associated with the sea level in 100 years during the future storm to that during Sandy, with the former minus the latter. As seen in the figure, in comparison with that of Hurricane Sandy, the maximum elevation during the storm with sea level in 100 years remains about the same, or, their difference is about zero, in most open sea areas as shown in Fig. 8. In the metropolitan NYC coastal regions, changes in the maximums occur, and they are mostly negative in values, e.g., a decrease in the maximum elevation. For instance, at the mouth of the Hudson River (Fig. 8b), the water elevation is essentially negative, or, the maximum elevation is lower by approximately 0.1 m than the maximum elevation during Hurricane Sandy. However, in the most of the other nearshore areas, particularly those that are south and north to the metropolitan region, including the Gulf of Maine, the Delaware Bay, and the Chesapeake Bay, the maximum water surface elevation becomes higher by approximately 0.1 m (Fig. 8b, e, f). In general, the maximum water surface elevation of the storm in the next 50 and 100 years exhibits characteristics similar to that of Hurricane Sandy (Qu 2017).

To quantitatively illustrate the SLR effects in water bodies near the seashore, Fig. 9 depicts a comparison of temporal evolution of surface elevation at two of the 18 observation stations, which are located near the coastlines. The evolution at these two stations
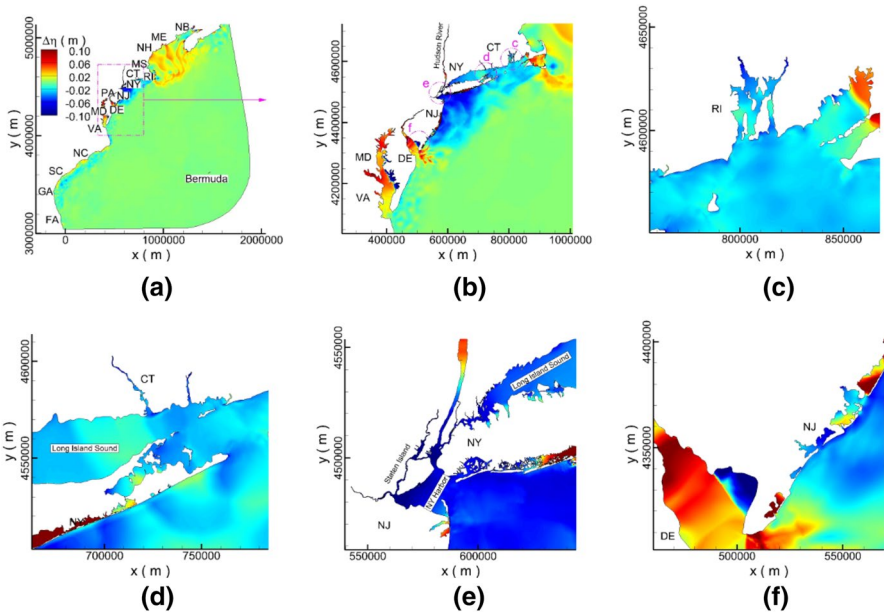
Fig. 8 Difference in maximum elevation of water surface in the condition of 100-year SLR during the storm to that of Hurricane Sandy

is representative of that at all 18 stations. The figures indicate that while in general water surface elevation during a storm event in the next 50 and 100 years with SLR is higher, and it presents a time history and pattern similar to that exhibited with Hurricane Sandy. The higher the SLR, the higher the water surface elevation becomes.

For more detailed information, the minimums and maximums of water surface at all of the 18 stations during the storms in reference to those during Hurricane Sandy are presented in Table 2. It is seen from the table that, at each station, the minimum elevation during a storm with SLR is lower than that in Sandy, and the maximum is higher than that in Sandy. This clearly indicates that SLR leads to stronger surges in terms of lowest and highest water surface elevation. Furthermore, the deviation in the maximum and minimum of elevation from those of Hurricane Sandy is roughly linear with SLR at most stations. For instance, at Station 8551762, the deviation of the minimum is -0.15 and -0.29 m, and that of the maximum is 0.22 and 0.44 m, respectively. In view that
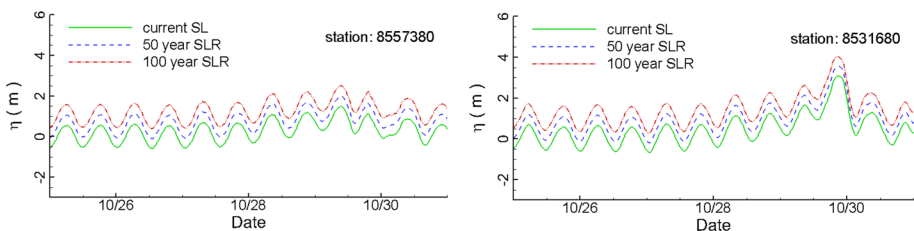
Fig. 9 Storm surge elevation at stations for water surface elevation

these stations are mostly located next to coastlines, such linearity is expected to be pre-vailing in the near seashore regions. Exception of such linearity occasionally occurs, such as at Station 8534720.

The difference between the maximum of depth-averaged current velocity during the storm events in condition of SLR in 100 years and that during Hurricane Sandy is plotted in Fig. 10. The figure shows that, the value is positive in many zones of the NYC metro coastal region, i.e., the maximum of velocity becomes higher by as much as 0.1 m/s than that during Hurricane Sandy. Such zones include the mouth of the Hudson River, the mouth of the Delaware Bay, south bank of NYC, and bank of NJ (Fig. 10b, e, f). However, decrease in the maximum, by as much as 0.1 m/s, also takes place in some zones, including the west end of the LIS and the upper region of the Delaware Bay (Fig. 10e, f). The change in the maximum exhibits strong locality. For instance, while the maximum increases in some parts of the mouth of the Hudson River, it also decreases in a few narrow zones there, e.g., Fig. 10e. Overall, the trends of the maxi-mum speed in SLR of 50 and 100 years are similar in most coastal region, although they are in opposite directions in some places, primarily in local zones.

Figure 11 presents the temporal evolution of current speed at the same two stations of Fig. 9. It is seen that the speed fluctuates in time at these two stations, and it reaches its maximum as Hurricane Sandy arrives. Also, interestingly, it remains about the same at all sea levels, and this indicates that SLR causes little difference in ocean current speed. Actu-ally, as seen in the following paragraph, in general, this is true at all 18 stations for water surface elevation.

At all 18 stations, similar to the pattern in water surface elevation as described above, the minimum value of current speed becomes lower and the maximum becomes higher as sea-level rises (Table 3). In general, the higher the sea level results in a lower of the mini-mum and in a higher of the maximum. Still there is linearity in the change of the minimum and the maximum values.

Table 2 Change in maximum and minimum in storm water surface in SLR conditions (Unit: m)
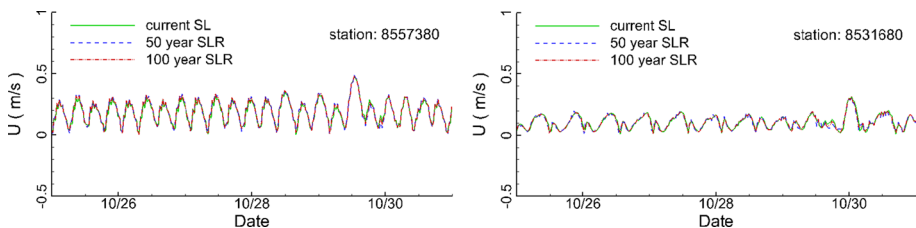
Station	8534720	8518750	8519483	8467150	8536110	8638863
$\Delta\eta_{min}$, 50 years	−0.10	−0.09	−0.16	−0.05	−0.05	−0.03
$\Delta\eta_{max}$, 50 years	0.08	0.06	0.15	0.05	0.03	0.03
$\Delta\eta_{min}$, 100 years	−0.12	−0.18	−0.32	−0.11	−0.07	−0.05
$\Delta\eta_{max}$, 100 years	0.11	0.13	0.30	0.11	0.06	0.07
Station	8551762	8516945	8557380	8540433	8510560	8465705
$\Delta\eta_{min}$, 50 years	−0.15	−0.09	−0.04	−0.17	−0.04	−0.06
$\Delta\eta_{max}$, 50 years	0.22	0.14	0.06	0.31	0.05	0.05
$\Delta\eta_{min}$, 100 years	−0.29	−0.17	−0.06	−0.32	−0.07	−0.11
$\Delta\eta_{max}$, 100 years	0.44	0.27	0.13	0.62	0.14	0.10
Station	8461490	8545240	8454049	8531680	8537121	8447930
$\Delta\eta_{min}$, 50 years	−0.05	−0.15	−0.08	−0.09	−0.10	−0.08
$\Delta\eta_{max}$, 50 years	0.06	0.35	0.08	0.07	0.15	0.05
$\Delta\eta_{min}$, 100 years	−0.09	−0.30	−0.12	−0.16	−0.20	−0.11
$\Delta\eta_{max}$, 100 years	0.09	0.69	0.13	0.14	0.33	0.10
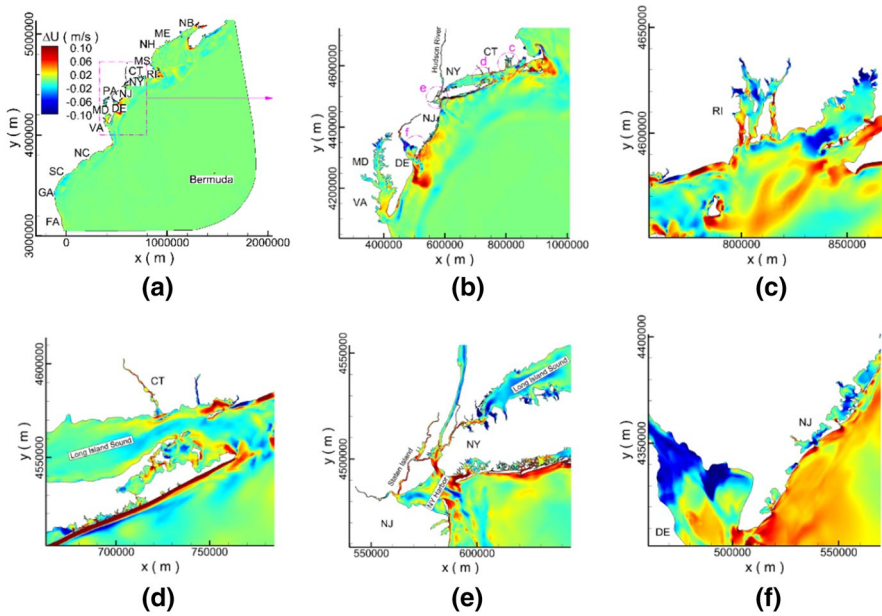
Fig. 10 Difference in maximum velocity in the condition of 100-year SLR during the storm to that of Hurricane Sandy

However, such linearity is in presence only at a few stations. An example is Station 8454049. Deviation in the current speed at this station in the minimum is −0.03 and −0.06 m/s, and that in the maximum is 0.05 and 0.11 m/s for in the condition of 50 and 100 years SLR, respectively, from those for the case of Hurricane Sandy. An interesting station is Station 8465705, at which the deviation in minimum and that in maximum remain the same at sea level of 50 and 100 years.

As seen in Fig. 12, as the sea level becomes higher, the maximum of wave height increases in most regions within the computational domain, but it also decreases in some zones. The figure indicates that wave height increases mostly in open water bodies at a certain distance away from the metropolitan NYC region. Overall the trends of increase and decrease in terms of regions are about the same in sea levels of 50 and 100 years (Qu 2017). A difference exists at a few regions, and one such place is the region above NYC in the computational domain, mostly in the water body north of NYC; as seen in Fig. 12a, the

Fig. 11 Storm surge velocity at stations for water surface elevation

Table 3 Change in maximum and minimum in current speed in SLR conditions (Unit: m)

| Station	8534720	8518750	8519483	8467150	8536110	8638863
ΔU_{min}, 50 years	− 0.04	− 0.06	− 0.03	− 0.02	− 0.06	− 0.04
ΔU_{max}, 50 years	0.06	0.05	0.07	0.01	0.06	0.03
ΔU_{min}, 100 years	− 0.12	− 0.09	− 0.05	− 0.03	− 0.12	− 0.09
ΔU_{max}, 100 years	0.12	0.16	0.13	0.02	0.11	0.10
Station	8551762	8516945	8557380	8540433	8510560	8465705
ΔU_{min}, 50 years	− 0.21	− 0.07	− 0.02	− 0.18	− 0.01	− 0.04
ΔU_{max}, 50 years	0.16	0.06	0.03	0.20	0.01	0.01
ΔU_{min}, 100 years	− 0.35	− 0.12	− 0.06	− 0.31	− 0.03	− 0.04
ΔU_{max}, 100 years	0.27	0.12	0.06	0.37	0.03	0.01
Station	8461490	8545240	8454049	8531680	8537121	8447930
ΔU_{min}, 50 years	− 0.06	− 0.08	− 0.03	− 0.03	− 0.16	− 0.12
ΔU_{max}, 50 years	0.07	0.18	0.06	0.03	0.15	0.19
ΔU_{min}, 100 years	− 0.12	− 0.06	− 0.06	− 0.06	− 0.34	− 0.20
ΔU_{max}, 100 years	0.09	0.27	0.11	0.06	0.30	0.36

maximum wave height of 100-years SLR in that water body is higher than that of Hurricane Sandy. However, as reported in Qu (2017), interestingly, the maximum wave height of 50-years SLR in the water body is lower in the hurricane. This illustrates the complexity of influence of SLR on surface waves.

The predicted temporal evolution of the significant wave height and peak wave period at a wave station in the New York harbor is plotted in Fig. 13. At this station, SLR presents a little effect on the significant wave height and peak wave period after the storm's arrival. A reason for the small change in wave is that, compared with the local water depth, the increase in still water elevation of 0.5 or 1.0 m is relatively small.

The simulation shows that, at most of the 10 wave stations (except Station 41013), the minimum and maximum of wave height present a pattern similar to that of the water surface elevation and current speed; the minimum of wave height becomes lower and the maximum becomes higher as the sea-level rises. This indicates that the wave height becomes more fluctuating in comparison with that during Hurricane Sandy in the SLR condition. Additionally, the maximum wave height for a storm event with SLR in 100 years is mostly higher than those for a storm event with SLR in 50 years at these wave stations (Qu 2017). However, linearity is rarely present in the deviation of water surface elevation and current speed for the storm events with SLR in 50 and 100 years compared to those of Hurricane Sandy (Table 4).

4.2 Storm surge and wave at different hurricane paths

To investigate the effects of hurricane paths on storm surges and waves in metropolitan NYC region, a detailed study has been carried out on the basis of more synthetic hurricanes. In particular, another eight synthetic hurricanes are generated by changing the path of Hurricane Sandy. Particularly, the synthetic hurricanes are the same to Sandy except that
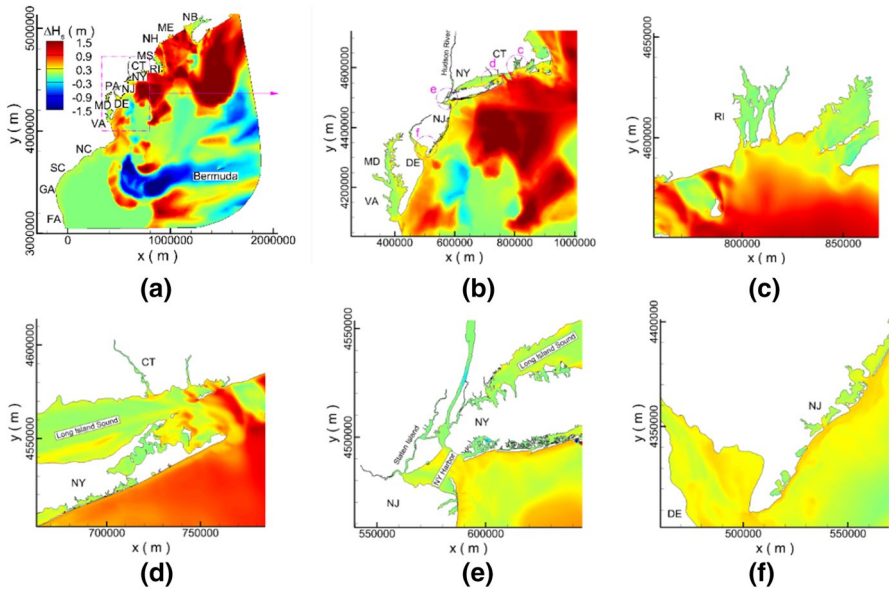
Fig. 12 Difference in maximum wave height in the condition of 100-year SLR during the storm to that of Hurricane Sandy
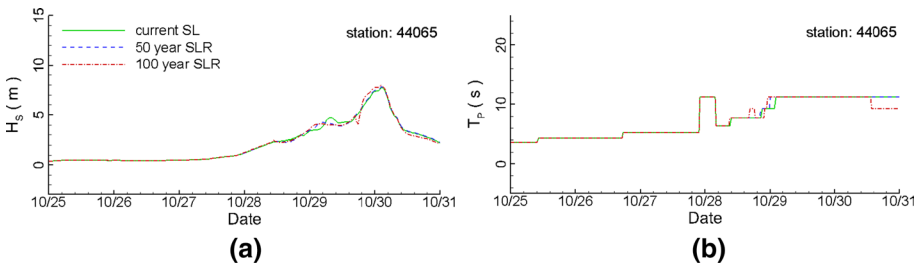
Fig. 13 Wave at an observation station. **a** Significant wave height. **b** Peak wave period

their wind fields result from a parallel shifting of that of Sandy. They are named as hurricanes with track 1–8 from south to north (Fig. 14). All synthetic hurricanes pass the metro NYC region, but through different locations (Table 5). For instance, the hurricane of track 4 makes its landfall at Rockaway Beach, New York, at Δlon = 0.4639°, Δlat = 1.1623°. Here Δlon and Δlat represent the difference of the landfall location of a synthetic hurricane to that of Hurricane Sandy in longitude and latitude, respectively.

As in the previous section, to assess the effects of hurricane tracks, the change in water surface elevation, current speed, and wave height in reference to those of Hurricane Sandy will be examined. The difference in the maximum surface elevation among all hurricanes with the eight tracks to that of Hurricane Sandy is presented in Fig. 15. The figure shows that, in general, the maximum water surface elevation increases in the metropolitan NYC and nearby regions. However, some regions experience a decrease of as much as − 0.34 m. The water surface elevation increase takes place at the south bank of NYC, the LIS, and the

Table 4 Differences in wave height at the wave stations in conditions of 50 and 100 years SLR (Unit: m)

Station	41013	44008	44020	44065	41002
$\Delta H_{s,min}$, 50 years	− 0.59	− 1.02	− 0.08	− 0.57	− 1.45
$\Delta H_{s,max}$, 50 years	1.94	1.40	0.23	0.63	1.23
$\Delta H_{s,min}$, 100 years	− 0.58	− 0.93	− 0.03	− 1.03	− 1.76
$\Delta H_{s,max}$, 100 years	1.31	1.48	0.32	0.72	0.69
Station	41048	44025	44096	44013	44039
$\Delta H_{s,min}$, 50 years	− 1.41	− 0.53	− 0.27	− 0.14	− 0.23
$\Delta H_{s,max}$, 50 years	1.23	0.91	0.68	0.18	0.19
$\Delta H_{s,min}$, 100 years	− 1.69	− 0.50	− 0.35	− 0.87	− 0.24
$\Delta H_{s,max}$, 100 years	0.97	1.13	0.72	0.70	0.49

Fig. 14 Paths of synthetic hurricanes passing the metro NYC region
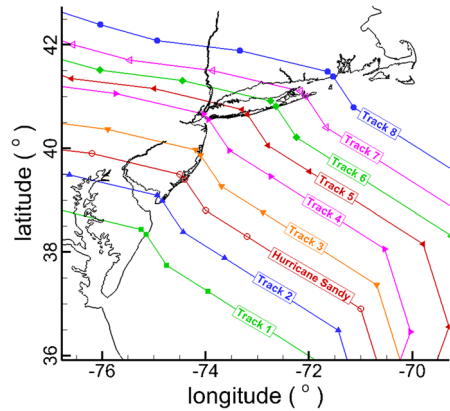
Delaware Bay (Fig. 15b, d, f). Within the latter two zones, the magnitude of the increase is as high as 2 m, and the area for such an increase is rather large. On the other hand, there is no apparent increase in other regions, including the NY harbor and the Chesapeake Bay

**Table 5** Landfall locations of the synthetic hurricanes in reference to that of Hurricane Sandy

Track index	Δlon (°)	Δlat (°)
Track 1	− 0.7473	− 1.0617
Track 2	− 0.4348	− 0.4121
Track 3	0.3072	0.4667
Track 4	0.4639	1.1623
Track 5	1.2079	1.2518
Track 6	1.7595	1.4113
Track 7	2.3382	1.6050
Track 8	2.8684	1.9863

areas (Fig. 15b, e). Such patterns are attributed to the tracks and landfall locations of the storms, and these results show their significant impacts on the storm surges.

Figure 16 shows the predicted temporal evolution of the surge elevation at two observation stations. As illustrated in the figure, different hurricane tracks lead to a pronounced difference in water surface elevation during the time of storms, from October 29–30. At different tracks, both peak values and curve patterns of the water surface elevation exhibit significant variations in time histories. For instance, the original track of Hurricane Sandy produces the largest surge elevation at Station 8534720, whereas Track 5 produces a much larger maximum surge elevation than that of Hurricane Sandy at Station 8465705. In addition, interestingly, instead of high-water surface elevation, low-water surface elevation occurs, such as at Station 8534720 in Track 4 and at Station 8465705 in Track 8.

The maximum and minimum of water surface elevation at all 18 stations for water surface elevation are given in Table 6. The table indicates that the minimum in water surface elevation associated with the eight tracks is lower than that during Hurricane Sandy at these stations, whereas their maximum is larger than that during Hurricane Sandy. The lowest value occurs at Station 8534720, and the highest value appears at Station 8551762. These results indicate that different tracks can generate stronger impact in terms of the magnitude of fluctuation in water surface elevation in comparison with that of Hurricane Sandy.

With regard to current velocity, it is observed that the increase in its maximum value primarily occurs along the coastline of NJ, the south bank of NYC, and the east end of LIS (Fig. 17b, d). In fact, current velocity as high as 1.9 m/s is observed in LIS. The change is not significant in most parts at the mouth of the Hudson River, the Delaware Bay, and the west end of LIS (Fig. 17e).
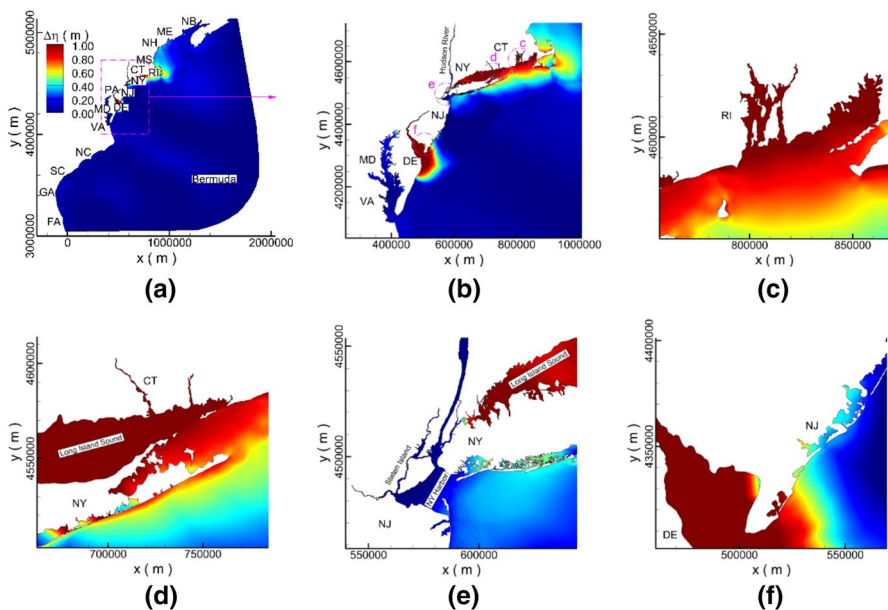
Fig. 15 Difference of maximum water surface elevation associated with different tracks to that of Hurricane Sandy
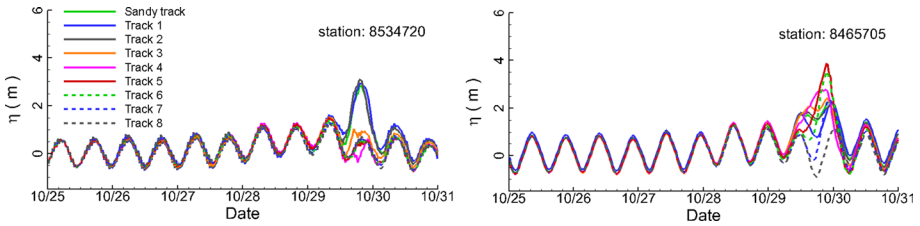
Fig. 16 Temporal evolution of surge elevation at observation stations

Figure 18 presents the time history of ocean current at two stations for water surface elevation. At Station 8534720, the temporal evolution associated with different tracks is distinct, and this shows that current speed is sensitive to hurricane tracks. Some tracks such as Track 1 lead to high speed, while the others such as Track 7 result in low speed. The current speed at Station 8465705 is not very sensitive to the alteration of hurricane tracks, although it exhibits certain differences for different tracks.

The ranges of change in current speed at the 18 stations are shown in Table 7. Similar to the pattern in water surface elevation, the minimum of current speed of the eight tracks becomes lower and the maximum current speed appears to be higher in comparison with those during Hurricane Sandy. The largest change in minimum current speed is at Station 8537121, and the largest change in maximum is at Station 844930. Such a change in current speed implies that different tracks could lead to stronger impact than that during Hurricane Sandy.

The distribution of maximum wave height for the eight hurricane tracks is shown in Fig. 19. Different from the water surface elevation and current speed, wave height increases significantly in a large portion within the computational domain, especially in open sea. In the metropolitan NYC region, such increase occurs along the south bank of NYC and within LIS (Fig. 19d). The maximum increase in the peak value of significant wave height is about 8.1 m at the south bank of NYC, at a location marked in red in Fig. 19e. Interestingly, there is little change in wave height in the NY harbor, south NJ, and the Delaware Bay (Fig. 19e, f).

Table 6 Minimums and maximums in water surface elevation, in m, associated with the eight tracks (Unit: m)

Station	8534720	8518750	8519483	8467150	8536110	8638863
$\Delta\eta_{min}$	− 2.95	− 2.75	− 3.17	− 2.73	− 1.44	− 0.72
$\Delta\eta_{max}$	0.65	0.63	0.44	1.44	1.48	0.41
Station	8551762	8516945	8557380	8540433	8510560	8465705
$\Delta\eta_{min}$	− 1.23	− 3.47	− 1.43	− 1.32	− 1.26	− 2.41
$\Delta\eta_{max}$	3.25	1.77	1.72	2.88	0.78	1.76
Station	8461490	8545240	8454049	8531680	8537121	8447930
$\Delta\eta_{min}$	− 1.74	− 1.20	− 1.63	− 2.72	− 1.27	− 0.62
$\Delta\eta_{max}$	1.27	2.56	1.42	0.58	3.22	1.15
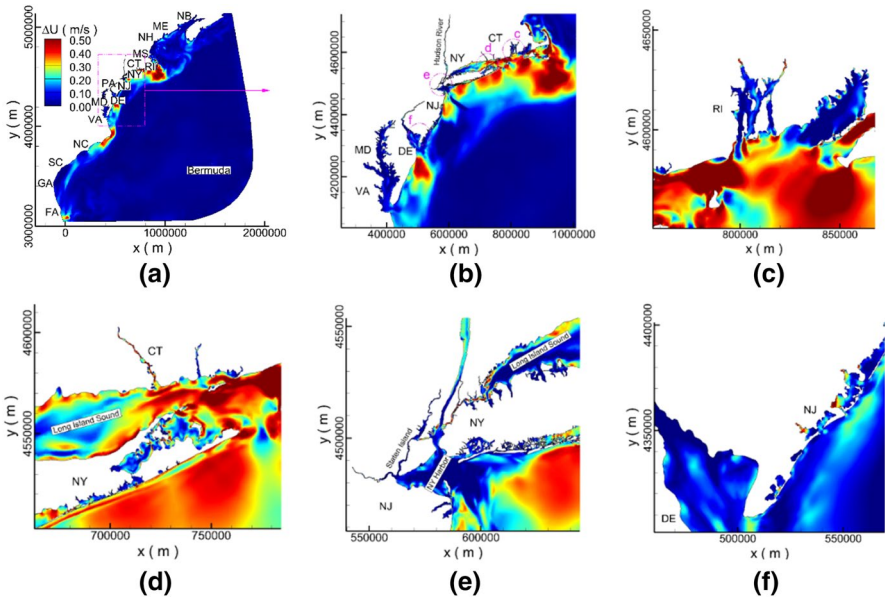
Fig. 17 Change of maximum in current speed associated with the eight tracks from that of Hurricane Sandy
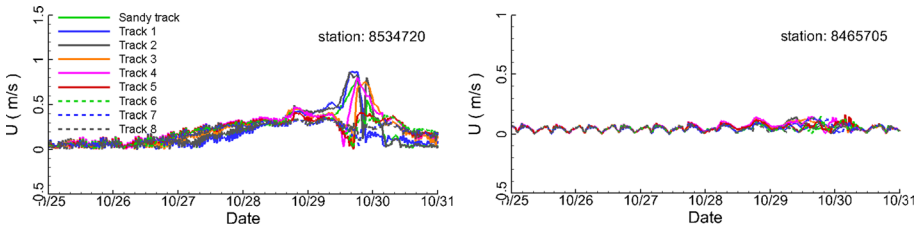
Fig. 18 Temporal evolution of depth-averaged current speed at observation stations for water surface

Table 7 Minimum and maximum in current speed associated with the eight tracks (Unit: m)

Station	8534720	8518750	8519483	8467150	8536110	8638863
ΔU_{min}	−0.70	−0.37	−0.33	−0.18	−0.43	−0.47
ΔU_{max}	0.53	0.67	0.35	0.21	0.36	0.36
Station	8551762	8516945	8557380	8540433	8510560	8465705
ΔU_{min}	−0.70	−0.43	−0.26	−0.60	−0.13	−0.10
ΔU_{max}	0.69	0.80	0.21	0.77	0.26	0.11
Station	8461490	8545240	8454049	8531680	8537121	8447930
ΔU_{min}	−0.16	−0.37	−0.13	−0.14	−0.89	−0.74
ΔU_{max}	0.45	0.57	0.47	0.47	0.73	0.94

The simulated evolution of wave height and its period at a station is shown in Fig. 20. As seen from this figure, the evolution of wave under different tracks of storms is distinct at this station; not only does the wave height present considerable variation, but also the peak wave period exhibits substantial fluctuation. Instead of a highest value, the wave height at this station may achieve the lowest value, such as in Track 8. This station is located in the New York harbor, and significant change in the wave at this location is an indication that the wave in this region may experience big change as a hurricane's path alters. However, interestingly, as discussed previously, both water surface elevation and current speed will not change much if the path is different. Furthermore, in comparison with that due to sea-level increase (Fig. 13), the change resulting from different tracks is much more pronounced, and this shows that hurricane tracks have stronger impact on waves than SLR.

As compared to the minimum and maximum change in the wave height during Sandy, the minimum change in wave height of the storms of eight tracks is lower, and the maximum change is higher (Table 8). A substantial change in the minimum change in the wave height, as much as 8 m, occurs at Station 44025, and the maximum change in significant wave height reaches as much as 9 m, at Station 41048. Compared those in Table 4, the numbers in Table 8 clearly indicate that wave height changes more substantially because of change of hurricane track than due to a rise in sea level.
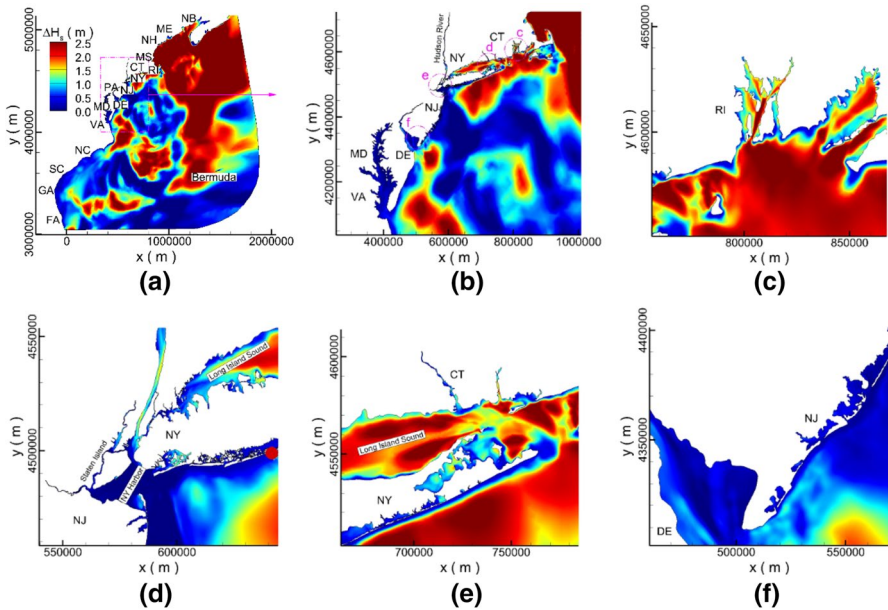

Fig. 19 Change of maximum in wave height associated with the eight tracks from that of Hurricane Sandy
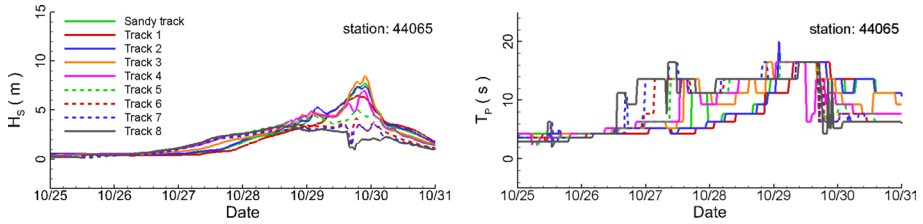
Fig. 20 Temporal evolution of wave at a wave station

5 Assessment of vulnerability of coastal bridges

5.1 Bridges and flow conditions

According to a bridge inventory as part of the National Bridge Inspection Standards (NBIS), which is documented by the US DOT FHA (FHA 2019), many of the bridges in the metropolitan NYC area are over coastal waters and their tributaries. In a case study by Shields (2016), NYC coastal bridges were prioritized based on hydraulic vulnerability to SLR using the NBIS inventory's criteria in three categories: (1) hydrologic and hydraulic factors, (2) structural and geotechnical factors, and (3) social importance factors. For this study, the prioritization criteria are modified, and, together with their thresholds and NBIS reference numbers, are listed in Table 9. When a bridge satisfies all of these criteria and the corresponding thresholds, it is considered "at risk" and then selected for further analysis in this study. Filtered by these criteria, 30 bridges (12 NJ bridges and 18 NY bridges) are selected for assessment of their vulnerability to future storm surge and wave (Fig. 21).

Parameters of the selected bridges are collected, and necessary simplification and approximation have been made on some of these parameters. A critical parameter is vertical clearance, which is the distance from a bridge deck to water surface elevation. In this study, the clearance of the 30 selected bridges is obtained from NBIS (FHA 2019). For each of the bridges, one pier is chosen as its representative pier. Parameters such as diameter or width are obtained from NBIS or measured from open sources such as Google Maps. It should be noted that some piers have lower and upper sections, which are different in shapes and sizes. For instance, a lower section, which is a base and is usually shorter in height, may be rectangle, and its width is used for scour estimation, while the upper section

Table 8 Maximums of wave height at wave stations in the case of with the eight tracks (Unit: m)

Station	41013	44008	44020	44065	41002
$\Delta H_{s,min}$	− 1.91	− 3.44	− 0.38	− 5.96	− 5.32
$\Delta H_{s,max}$	2.33	4.29	1.48	1.37	5.51
Station	41048	44025	44096	44013	44039
$\Delta H_{s,min}$	− 5.86	− 7.77	− 0.96	− 1.19	− 1.70
$\Delta H_{s,max}$	8.95	2.17	0.73	5.49	2.23

Table 9 Bridge selection criteria

Category	Criterion	Thresholds	NBIS reference
Hydrologic and hydraulic factors	If bridge satisfies at least one of the four criteria	Bridge is scour critical	Item 113 is 2 or 3
		Bridge has weak channel protection	Item 61 <=3
		Inadequacy waterway	Item 71 <=3
		Large number of approach spans	Item 46 > 3
Structural and geotechnical factors	If bridge satisfies at least one of the two criteria	Old bridge	Item 27 < 1940
		Poor structural evaluation	Item 67 < 3
Social importance factors	(1) ADT > 100,000, detour > 5 km or (2) ADT > 10,000 detour > 10 km	Large average daily traffic	Item 29
		Long detour length	Item 19

may be circular, whose diameter is adopted in force computation. For a pier with an upper section of noncircular cross section, a surrogate circle is considered, and the width of the pier is taken as its diameter.

These parameters are listed in "Appendix A." The water surface elevation, flow speed, wave height, and other flow-related parameters at the bridges are extracted from the simulation as described in previous sections.

5.2 Assessment methods

Standard engineering practice is adopted to estimate the vulnerability of selected 30 bridges. The hydrodynamic impact of water on bridge piers is evaluated according to (Wienkea and Oumeraci 2005)

$$F = F_D + F_I + F_S \tag{4}$$

where F_D, F_I, and F_S are drag force, inertia force, and slamming force, respectively. The drag force in Eq. (4) is evaluated by (McConnell et al. 2004).

$$F_D = \frac{1}{2}\rho C_D D V^2 y \tag{5}$$

where C_D is the drag coefficient, which is approximated as 1 (McConnell et al. 2004), ρ is water density ($= 1000$ kg/m^3), D is the diameter of a bridge pier, V is the velocity at the pier, and y represents the depth of water in front of the pier. The inertia force is calculated as (McConnell et al. 2004)

$$F_I = \rho C_M D \dot{V} y \tag{6}$$

where C_M is the inertia coefficient with a value of 2. $\dot{V}$ is acceleration of a fluid particle at the pier and is approximated as $g \, \pi \, H/L$, where g is the acceleration because of gravity ($= 9.8$ m/s^2), H the wave height, and L the wave length. The slamming force is computed as,

$$F_S = \frac{1}{2}\rho\lambda C_S D C_b^2 \eta_b \tag{7}$$

in which λ is the curling factor with value of 0.46, C_S is the slamming factor with value of π (Wienkea and Oumeraci 2005), C_b is the wave celerity and is approximated by $\sqrt{gy}$.

According to HEC-18, the scour depth, y_s, at the front of a bridge pier is estimated by a model suggested by Arneson et al. (2012)as

$$\frac{y_s}{y} = 2 \cdot K_1 \cdot K_2 \cdot K_3 \cdot \left(\frac{W}{y}\right)^{0.65} \cdot \text{Fr}^{0.43} \tag{8}$$

where W is the pier width, K_1 is the correction factor for pier nose shape, K_2 is the correction factor for the angle of attack flow, K_3 is the correction factor for bed condition, and $\text{Fr} = V/\sqrt{gy}$, being the Froude number at the immediately upstream of the pier. In this study, K_2 is set as 1.0, while both K_1 and K_3 are determined according to their cross-sectional shapes, and they range between 0.9 and 1.1.

A bridge may be at risk of structural damage and failure, such as deck unseating due to the impact of extreme surge waves, and this study utilizes a parameterized formula developed to estimate the probability of such failure, p, in concrete girder bridges located in South Carolina (Kameshwar and Padgett 2014),

$$p\big(\text{fail}|S, H, H_s\big) = \frac{1}{1 + \exp\big(l_x\big)} \tag{9}$$

in which l_x represents the logarithm of odds in favor of a bridge failure, and

$$l_x = 2.71 + 3.47(H_B - S) - 1.59H - 0.17H(H_B - S) + 0.22(H_B - S)^2 - 0.05H^2$$
(10)

Here S is the inundation depth, H the wave height, and H_B the bridge clearance.

It is noted that vulnerability assessment of bridges is challenging because of its dependence on numerous factors. Although approaches described above for assessment of hydrodynamic, scour, and structural failure are based on standard engineering practice, they have limitations because of simplifications in parameters as well as limitations in the equations. For instance, Eq. (8) assumes sandy seabed only, while other bottom types are present and often scour countermeasures are implemented at most bridges. Additionally, it considers a unidirectional steady flow and scour at equilibrium state, while a coastal bridge experiences unsteady, alternative-direction tides. Therefore, the scour depth estimated by Eq. (8) may not be the actual pier scour depth at a bridge.

5.3 Assessment for vulnerability of bridges

The hydrodynamic load acting on the piers of all selected bridges is plotted for all scenarios of sea levels and hurricane tracks see Fig. 22a. In this figure, only drag and inertia forces are included, and maximum velocity and surface elevation are used in their computations, which are extracted from simulated solutions at elements near the bridges. The figure shows that in all scenarios with hurricanes, the magnitude of the load increases substantially in comparison with that associated with the normal sea level and without a storm before Sandy. For most bridges, the load is approximately 200 KN or less. However, it is much higher at two bridges, particularly NY-5521217/18 and NY-5522507, which are the Verrazano Narrows and the George Washington Bridge, respectively. The load at the former and the latter occurs during SLR of 100 and 4, respectively, and both are as high as about 700 kN. This figure also indicates that, almost at all bridges, the maximum load is not during Hurricane Sandy. Rather, some other more severe scenarios may lead to a load larger than during Superstorm Sandy. Figure 22b shows histogram of loads at piers of all bridges for a comprehensive understanding.

A potential worst case occurs when slamming force is generated at a bridge pier because of wave breaking. The hydrodynamic load in such a situation is evaluated as in Fig. 23. It is seen that the load distribution among these piers is similar to that with no presence of slamming. However, it increases dramatically. Still the two bridges mentioned above bear the largest load, which is 5500 and 4000 kN at NY-5521217/5521218 and NY-5522507, respectively. The significant increase in the load indicates the danger of wave slamming. Discussion on the load of additional bridges can be found in Tang and Qu (2018).

The scour depth at piers in all scenarios is plotted in Fig. 24. In view of inundation of storm surges, maximum water depth and half of the maximum velocity during storms are used to compute the scour depth. The figure shows that most bridges will experience a pier scour depth ranging from one to eight meters. The first three bridges with the worst scour are, again, NY-5522507, NY-5521217, and NY-5521209 with scour depth
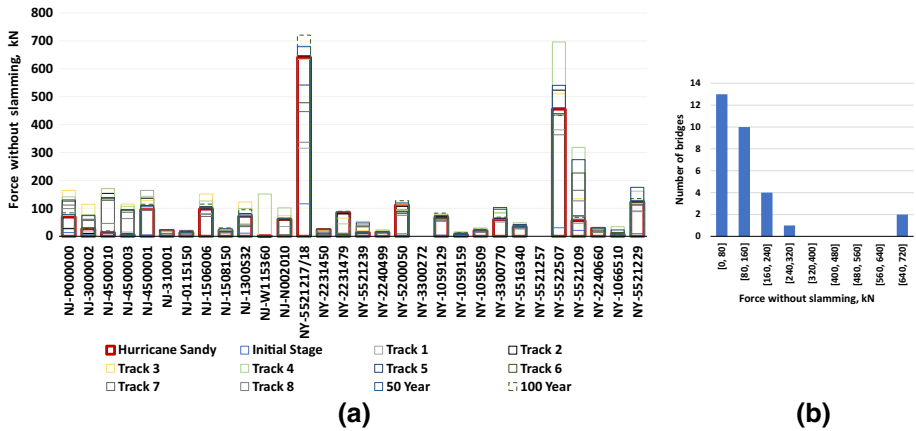
Fig. 22 Maximum of hydrodynamic loads, without slamming. **a** All bridges. **b** Histogram of loads

of 14, 11, and 10 m approximately, respectively. Again, this figure shows that the pier scour is deeper in some scenarios than that during Hurricane Sandy at all bridges. The histogram of pier scour is presented in Fig. 24b, which shows an overview of scour at all piers under consideration. More discussion on scour at bridges is available in Tang and Qu (2018). As noted previously, the pier scour depth is estimated by assuming sandy bed, and it may not be the actual scour. For instance, at the piers of George Washington Bridge, there are walls of protection around them. Nevertheless, the estimate of them in the two figures reflects the potential influence of storms on scour at these bridges.

An assessment of risk for bridge failure based on Eq. (9) is presented in Fig. 25. It is seen that the probability of failure at all bridges is negligible, except at bridges NY-2240499 and NY-2231479, which are Crossbay Blvd North Channel and Mill Basin Bridge, respectively. At the former, the probability is relatively small; it is about 0.02 in scenario of sea-level rise in 100 years. At the latter, the probability of damage is at least 0.1 in a quite few scenarios, and it is over 0.5 in the scenario of sea-level rise in
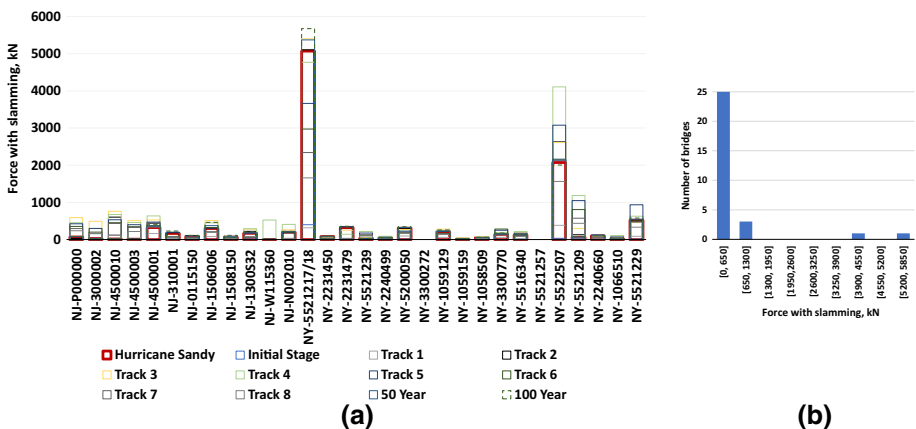

Fig. 23 Maximums of hydrodynamic loads, with slamming. **a** All bridges. **b** Histogram of loads
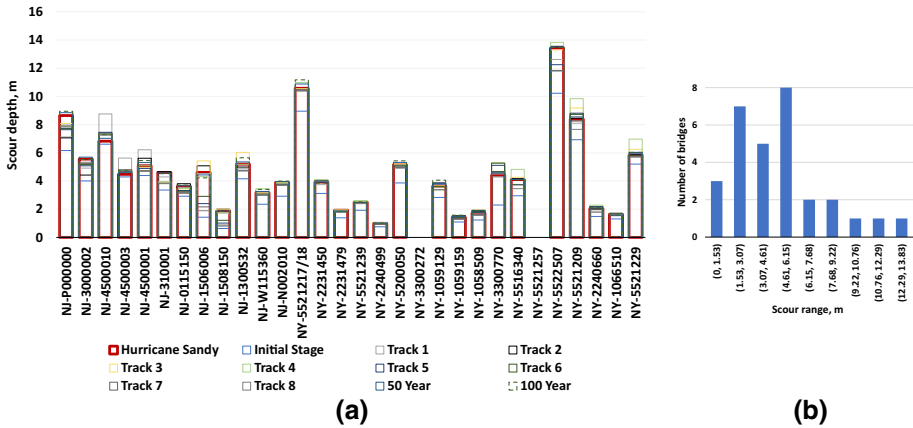
Fig. 24 Pier scour depths. **a** All bridges. **b** Histogram of scour depths
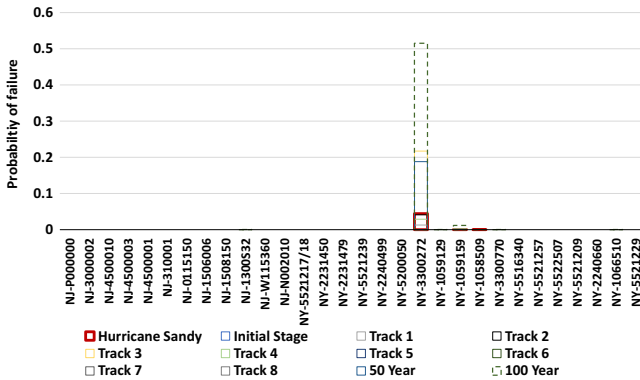

Fig. 25 Probability of damage at all bridges

100 years. In fact, the inundation depth at this bridge for sea-level rise in 100 years is 5.72 m, while the bridge clearance is 4.98 m. Since the inundation depth is larger than the bridge clearance, overtopping of water is expected at the bridge. Again, it is seen in the figure that some scenarios are worse than Hurricane Sandy in terms of the probability of damage.

6 Concluding remarks

A hindcast study has been performed for storm surges and waves along the coast of metropolitan NYC region during Hurricanes Sandy. Synthetic hurricanes, as perturbation to the sea level and the track of Hurricane Sandy, are considered, and their storm surges and

waves are predicted as potential future scenarios. On the basis of the prediction, hydrodynamic load, pier scour, and the probability of bridge failure are assessed using engineering approaches. This findings and further studies are discussed as follows:

1. Storm surges and waves are affected by sea-level rise and hurricane tracks in the NYC metropolitan region, and such influence is complex in quantitative and qualitative aspects.
2. Surges and waves generated by the synthetic scenarios with the change in sea level and hurricane track can be much stronger than those during Hurricane Sandy.
3. With regard to hydraulic vulnerability of bridges to hydrodynamic loads, pier scour depths, and structural failure probability, some of the scenarios are worse than those during Hurricane Sandy for the NYC metropolitan region. The failure probability for all considered bridges, except for a local bridge, is negligible.

Since various factors with uncertainties are involved, predicting storm surges and waves and the resulting impact to the coastlines in the region remains challenging, and limitations of this study need be addressed in future studies. In this study, all scenarios under consideration are based on Hurricane Sandy; however, more variations are possible as future scenarios. Additionally, finer tuning of the simulation, such as collecting more observation data (e.g., ocean current speed) along the coastlines, adopting higher mesh resolution, and including more details of bridge parameters, could enhance the confidence level of the results. The assessment of hydrodynamic impact on bridges follows routine engineering approaches, which has limitations, especially in dealing with extreme situations. For instance, the predicted scour depth seems unreasonably large, and this could be due to limitations of the formulas adopted. Also, the hydrodynamic load on a bridge pier involves complex physical processes, and more advanced modeling tools with multiscale and multiphysics capabilities, such as that developed by Qu et al. (2019a, b), are desirable for more reliable assessment. Additionally, the failure probability of bridges is estimated using a formula developed for a particular type of bridges in a specific region, and its applicability may be limited. A fluid–structure interaction model such as LS-DYNA would be helpful in increasing the reliability of results on hydrodynamic effects and bridge failure probabilities (Nguyen et al. 2005). All of these issues shall be considered in our future work.

Compliance with ethical standards

Conflict of interest The authors declare that they have no conflict of interest.

Appendix A: Measured and blended wind fields at wind stations
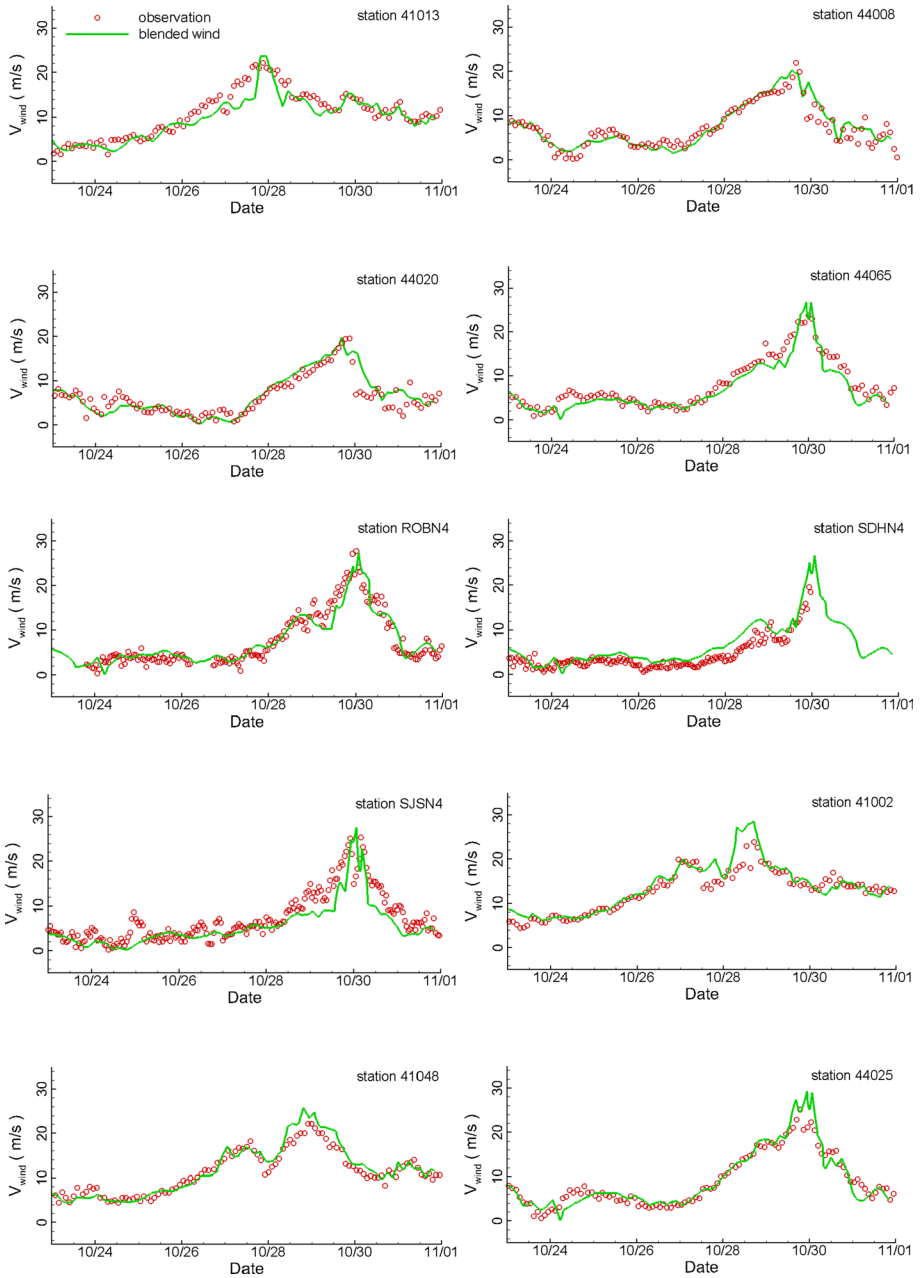
See Figs. 26, 27, and 28.

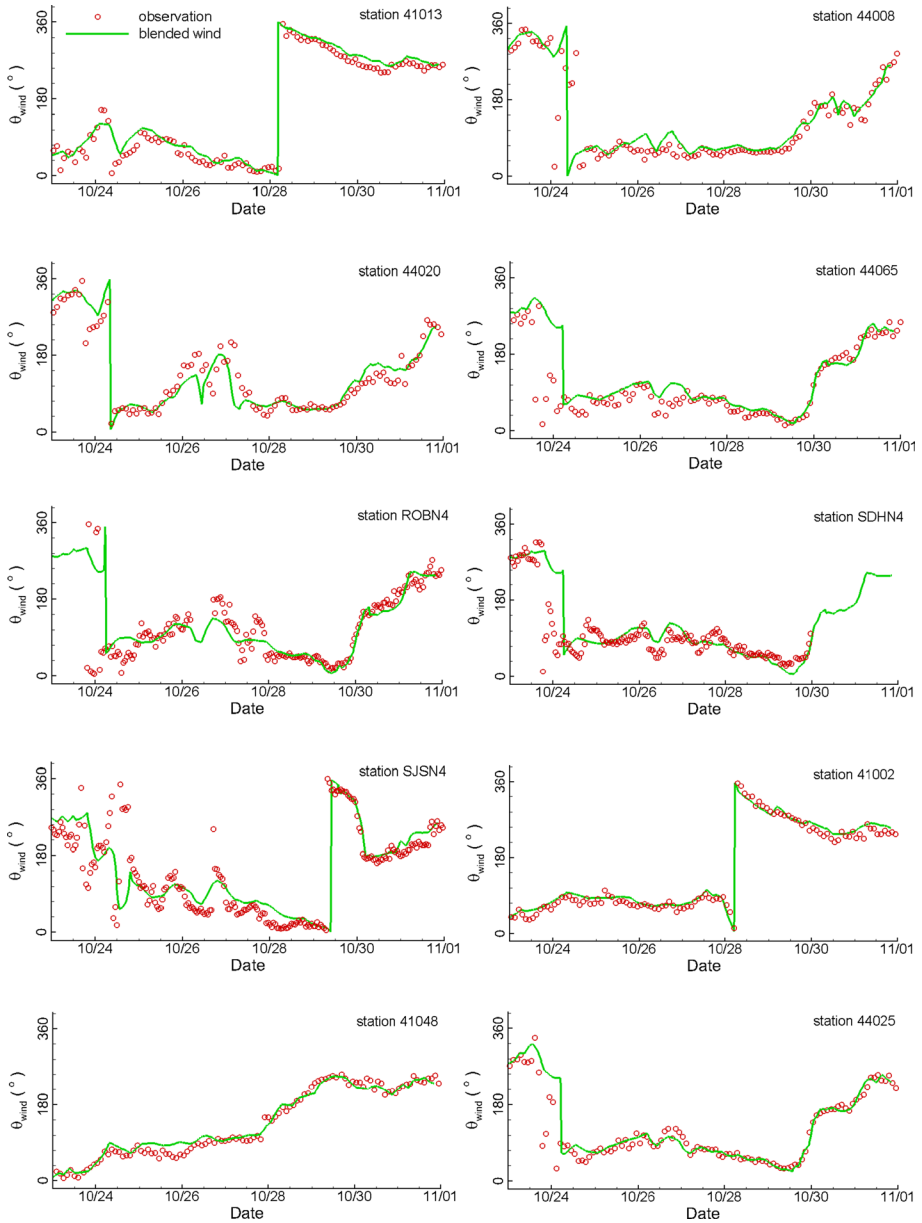Fig. 26 Comparison in the speed of the observed and the blended wind fields

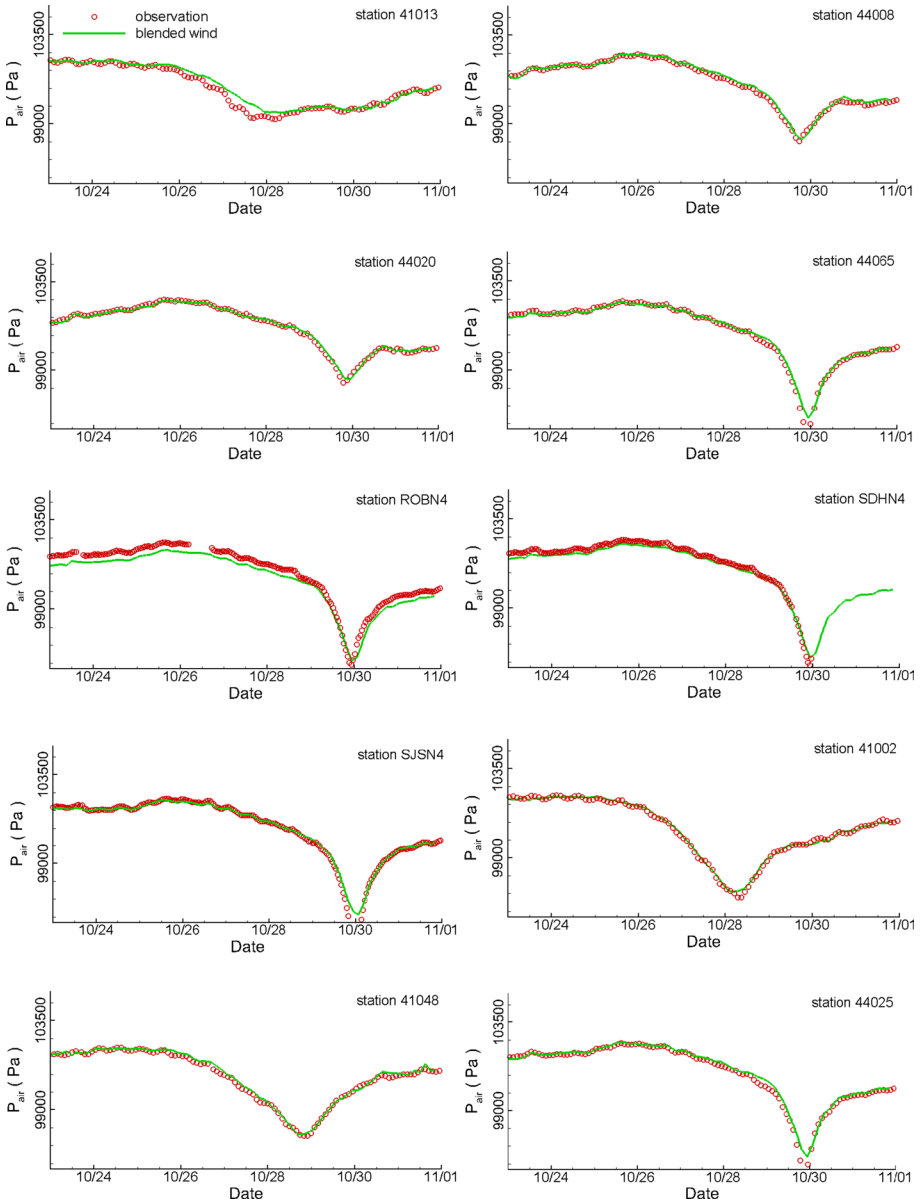**Fig. 27** Comparison in the direction of the observed and the blended wind fields

Fig. 28 Comparison in the pressure of the observed and the blended wind fields
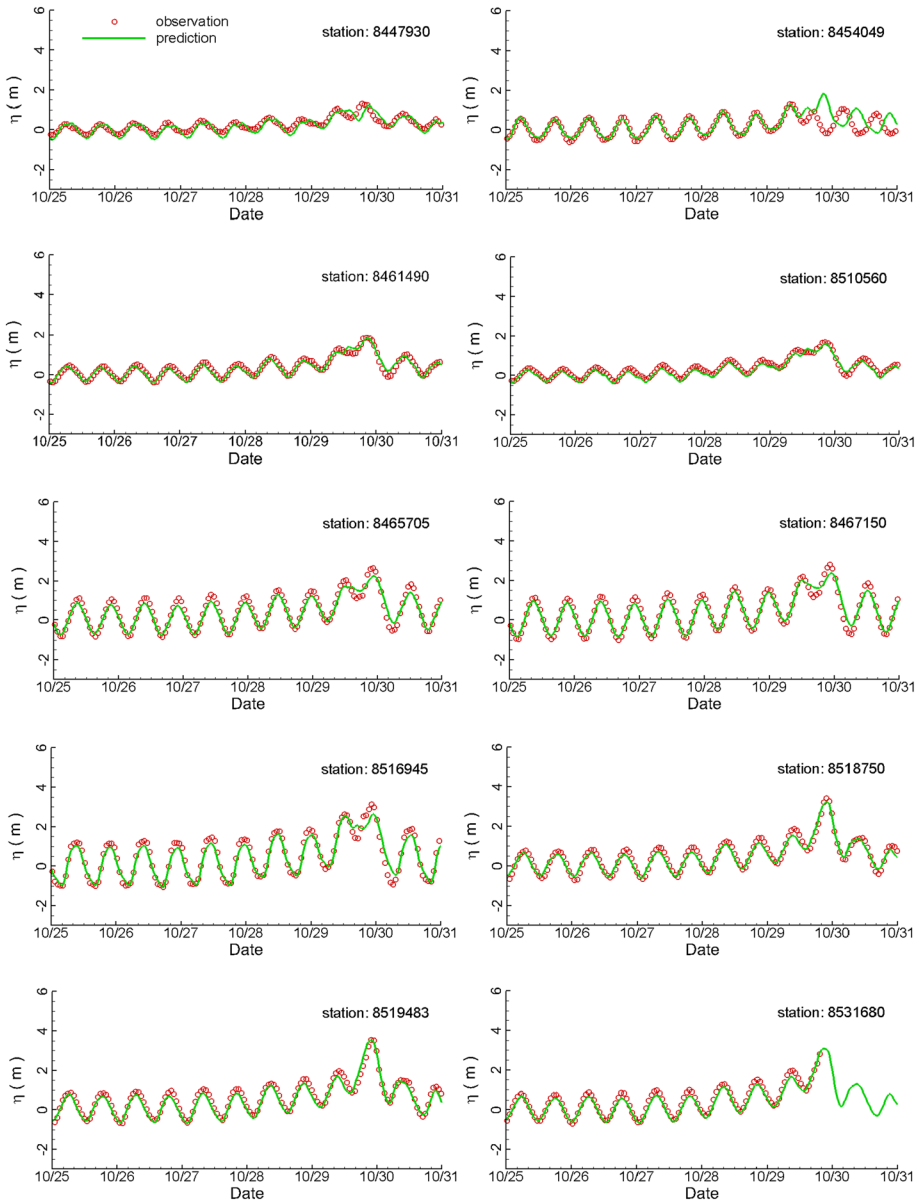
Fig. 29 Comparison of computed and observed water surface elevation

Appendix B: Simulated and measured water surface elevation and wave during Hurricane Sandy
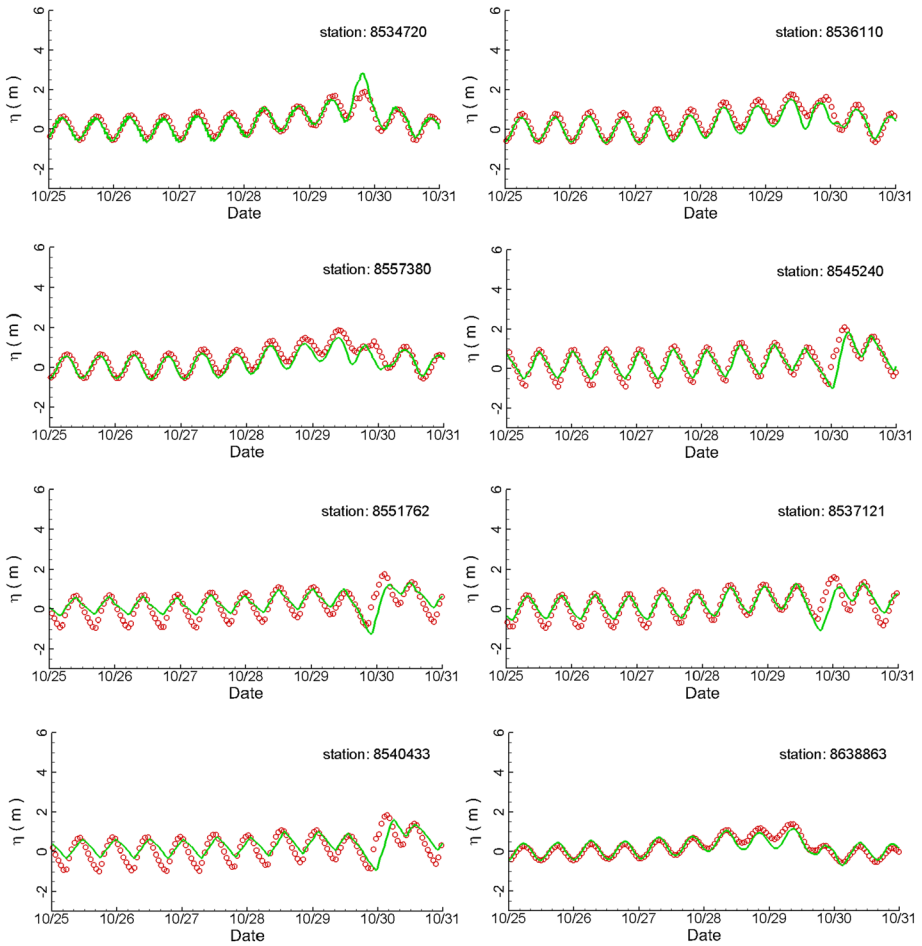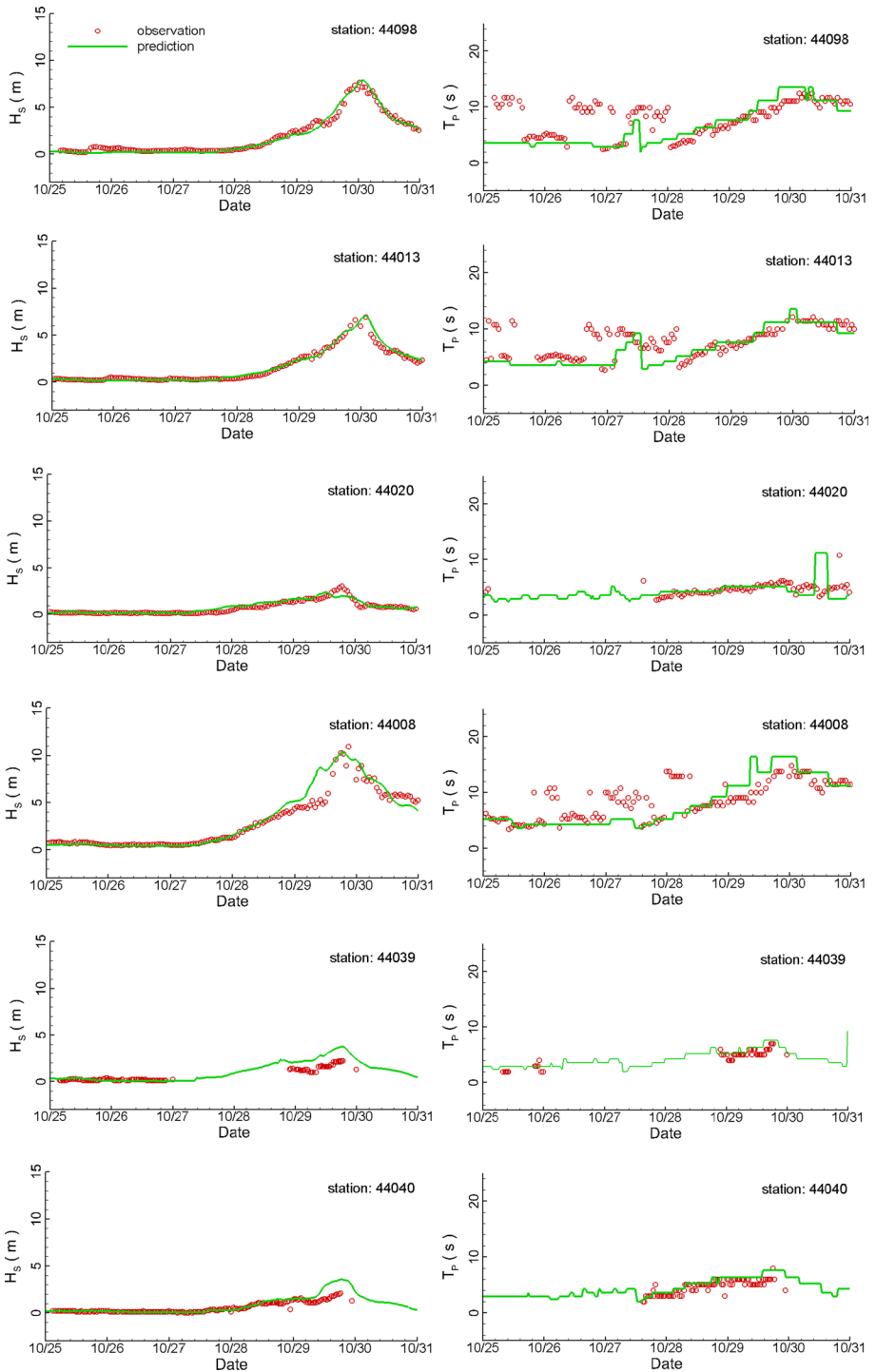
See Figs. 29 and 30.

Fig. 29 (continued)

Fig. 30 Comparison in significant wave height and peak wave period obtained with simulation and observation
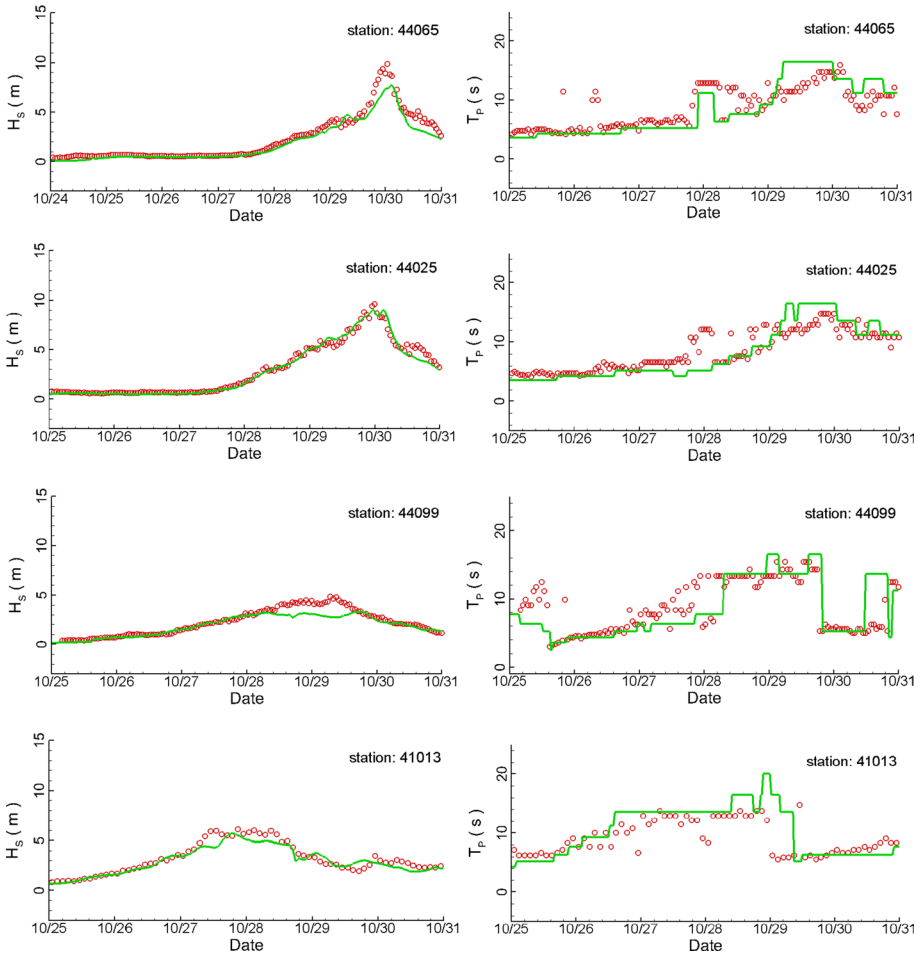
Fig. 30 (continued)

Appendix C: Bridge parameters

Bridge ID	Name/Location	Z_b (m)	H_b (m)	D (m)	W (m)
NJ-P000000	Turnpike Connector Bridge	−7.09	49.43	7.11	11.83
NJ-3000002	Burlington Bristol Bridge	−7.79	50.05	4.2	8.07
NJ-4500010	Ben Franklin Bridge	−8.02	48.23	10.92	17.25
NJ-4500003	Walt Whitman Bridge	−10.67	57.25	7.17	11.03
NJ-4500001	Commodore Barry Bridge	−6.38	63.73	8.69	10.29
NJ-310001	Ocean City-Longport Bridge	−2.62	23.02	2.46	7.05
NJ-0115150	Brigantine Bridge	−2.00	20.79	1.77	6.24
NJ-1506006	Barnegat Bay Bridge	−2.54	11.79	10.03	10.03
NJ-1508150	Mathis Bridge	−2.01	10.96	2	2
NJ-1300S32	Shrewsbury River Bridge	−3.70	10.27	5.3	6.7
NJ-W115360	NJ TPK Hackensack River Bridge	−5.14	21.27	11.29	11.29
NJ-N002010	Newark Bay Bridge	−3.32	45.24	5.9	7.69
NY-5521217/ NY-5521218	Verrazano Narrows (Upper and Lower)	−15.26	85.32	16	23.99
NY-2231450	Gerritsen Inlet Bridge	−2.26	13.74	1.84	8.85
NY-2231479	Mill Basin Bridge	−4.00	15.35	6.84	6.84
NY-5521239	Crossbay Vets Memorial Bridge	−3.32	20.17	3.08	3.08
NY-2240499	Crossbay Blvd North Channel	−2.90	11.59	1.26	1.26
NY-5200050	Atlantic Beach Bridge	−3.23	11.43	5.76	5.76
NY-3300272	Long Beach Road and Barnum Isld Creek	−2.00	4.98	0	NA
NY-1059129	Meadowbrook State Parkway Bridge	−3.47	10.33	4.74	4.74
NY-1059159	False Channel on Meadowbrook State Pkwy	−3.92	7.99	1.24	1.24
NY-1058509	Goose Creek Bridge	−3.04	8.20	1.39	1.39
NY-3300770	Narrow Bay Bridge	−2.25	7.81	5.92	5.92
NY-5516340	Gov. Mario M. Cuomo Bridge	−4.45	28.71	2.76	8.64
NY-5521257	Henry Hudson Bridge	−5.03	49.05	0	NA
NY-5522507	George Washington Bridge	−11.47	76.91	19	28.67
NY-5521209	Tri-borough Harlem River Lift Bridge	−16.28	58.02	9.43	14.69
NY-2240660	Rikers Island Bridge	−4.96	21.57	2.14	5.31
NY-1066510	BE Service Rd Westchester Creek Bridge	−3.96	10.14	2.39	3.85
NY-5521229	Bronx Whitestone Bridge	−7.51	49.59	6.43	10.08

Z_b is the bed elevation, H_b is the bridge clearance, D is the pier diameter, and W is its width

References

Apollonio C, Bruno MF, Iemmolo G, Molfetta MG, Pellicani R (2020) Flood risk evaluation in ungauged coastal areas: the case study of Ippocampo (southern Italy). Water 12:1466

Arneson LA, Zevenbergen LW, Lagasse PF, Clopper PE (2012) Evaluating Scour at Bridges, FHWA-HIF-12-003, Fifth Edition, U.S. Department of Transportation Federal Highway Administration

Bennett VCC, Mulligan RP, Hapke CJ (2018) A numerical model investigation of the impacts of Hurricane Sandy on water level variability in great South Bay, New York. Cont Shelf Res 161:1–11

Blumberg AF, Georgas N, Yin L, Herrington TO, Orton PM (2015) Street-scale modeling of storm surge inundation along the New Jersey Hudson River waterfront. J Atmos Ocean Technol 32:1486–1497

CNNlibrary (2016) Hurricane Sandy fast facts. http://www.cnn.com/2013/07/13/world/americas/hurricane-sandy-fast-facts/, Wed Nov 2 2016

Coch NK (2015) Unique vulnerability of the New York-New Jersey metropolitan area to hurricane destruction. J Coast Res 31:196–212

Edson J (2009) Review of air-sea transfer processes, paper presented at ECMWF Workshop 2008 on Ocean-Atmosphere Interactions, Reading, England

Egbert G, Bennett A, Foreman M (1994) Topex/Poseidon tides estimated using a global inverse model. J Geophys Res 24:821–852

Fairall CW, Bradley EF, Hare JE, Grachev AA, Edson JB (2003) Bulk parameterization of air-sea fluxes: updates and verification for the COARE algorithm. J Clim 16:571–591

Federal Highway Administration (2019) Bridges and structures. https://www.fhwa.dot.gov/bridge/nbi.cfm

Hallett R, Johnson ML, Sonti NF (2018) Assessing the tree health impacts of salt water flooding in coastal cities: a case study in New York City. Landsc Urban Plan 177:171–177

Hatzikyriakou A, Lin N (2017) Simulating storm surge waves for structural vulnerability estimation and flood hazard mapping. Nat Hazards 89:939–962

Hu K, Chen Q, Wang HQ, Hartig EK, Orton PM (2018) Numerical modeling of salt marsh morphological change induced by Hurricane Sandy. Coast Eng 132:63–81

Jacob AK, Deodatis G, Atlas J, Whitcomb M, Lopeman M, Markogiannaki O, Kennett Z, Morla A, Leichenko R, Vancura P (2011) Transportation, "Responding to climate change in New York State: the ClimAID integrated assessment for effective climate change adaptation in New York State". Ann N Y Acad Sci 1244(1):299–362

Kameshwar S, Padgett JE (2014) Multi-hazard risk assessment of highway bridges subjected to earthquake and hurricane hazards. Eng Struct 78:154–166

Kantamaneni K (2016) Coastal infrastructure vulnerability: an integrated assessment model. Nat Hazards 84:139–154

Kress ME, Benimoff AI, Fritz WJ, Thatcher CA, Balanton BO, Dzedzits E (2016) Modeling and simulation of storm surge on Staten Island to understand inundation mitigation strategies. J Coast Res 76:149–161

Large WG, Pond S (1981) Open ocean momentum fluxes in moderate to strong winds. J Phys Oceanogr 11:324–336

Lin N, Emanue KA, Smith JA, Vanmarcke E (2010) Risk assessment of hurricane storm surge for New York City. J Geophy Res 115:D18121

Malik S, Lee DC, Doran KM, Grudzen CR, Worthing J, Portello I, Goldfrank LR, Smith SW (2018) Vulnerability of older adults in disasters: emergency department utilization by geriatric patients after hurricane sandy. Disaster Med Public Health Prep 12:184–193

Markogiannaki O (2019) Climate change and natural hazard risk assessment framework for coastal cable-stayed bridges. Front Built Environ 5:116

McConnell K, Allsop W, Cruickshank I (2004) Piers, jetties and related structures exposed to waves—guidelines for hydraulic loading. Thomas Telford Publishing, London

Meixler MS (2017) Assessment of hurricane sandy damage and resulting loss in ecosystem service in a coastal-urban setting. Ecosyst Serv 24:28–46

Miles T, Seroka G, Glenn S (2017) Coastal ocean circulation during Hurricane Sandy. J Geophys Res-Oceans 122:7095–7114

Nguyen MQ, Elder DJ, Bayandor J, Thomson RS, Scott ML (2005) A review of explicit finite element software for composite impact analysis. J Compos Mater 39:375–386

NOAA CSC (2020) https://shoreline.noaa.gov/data/datasheets/composite.html

NOAA ETOPO1 (2020) https://www.ngdc.noaa.gov/mgg/global/

NOAA NCEI (2020) https://www.ncdc.noaa.gov/data-access/model-data/model-datasets/north-american-regional-reanalysis-narr

NOAA NDBC (2020) https://www.ndbc.noaa.gov/

NOAA NGDC (2020) https://www.ngdc.noaa.gov/

NOAA SCR (2020) https://www.ngdc.noaa.gov/mgg/shorelines/shorelines.html

Orton PM, Hall TM, Talke SA, Blumberg AF, Georgas N (2016) A validated tropical-extratropical hazard assessment for new york harbor. J Geophys Res-Oceans 121:8904–8929

Parker B, Milbert D, Hess K, Gill S (2003) National VDatum-the implementation of national vertical datum transformation databased. In: Proceedings of the U.S. hydrographic conference, Biloxi, Mississippi, Mar 24–27

Pfeffer WT, Harper JT, O'Neel SO (2008) Kinematic constraints on glacier contributions to 21st century sea-level rise. Science 321:1340–1343

Powell MD, Houston SH, Reinhold TA (1996) Hurricane Andrew's landfall in South Florida Part I: standardizing measurements for documentation of surface wind fields. Weather Forecast 11:304–328

Powell MD, Houston SH, Amat LR, Morisseau-Leroy N (1998) The HRD real-time hurricane wind analysis system. J Wind Eng Ind Aerodyn 77–78:53–64

Powell M, Shchepetkin AF, Sherwood CR, Signell RP, Warner JC, Wilkin J (2008) Ocean forecasting in terrain-following coordinates: formulation and skill assessment of the regional ocean modeling system. J Comput Phys 227:3595–3624

Powell MD, Murillo S, Dodge P, Uhlhorn E, Gamache J, Cardone V, Cox A, Otero S, Carrasco N, Annane B, St. Fleur R (2010) Reconstruction of Hurricane Katrina's wind fields for storm surge and wave hindcasting. Ocean Eng 37:26–36

Qi J, Chen C, Beardsley RC, Perrie W, Cowles GW, Lai Z (2009) An unstructured grid finite-volume surface wave model (FVCOM-SWAVE): implementation, validations and applications. Ocean Model 28:153–166

Qu K (2017) Computational study of hydrodynamic impact by extreme surge and wave on coastal structure. Ph.D. thesis, The City College of New York, New York, USA

Qu K, Tang HS, Agrawal A (2019a) Integration of fully 3D fluid dynamics and geophysical fluid dynamics models for multiphysics coastal ocean flows: simulation of local complex free-surface phenomena. Ocean Model 135:14–30

Qu K, Sun WY, Tang HS, Jiang CB, Deng B, Chen J (2019b) Numerical study on hydrodynamic load of real-world tsunami wave at highway bridge deck using a coupled modeling system. Ocean Eng 192:106–486

Shields GM (2016) Resiliency planning: prioritizing the vulnerability of coastal bridges to flooding and scour. Proc Eng 145:340–347

Shultz JM, Kossin JP, Shepherd JM, Ransdell JM (2019) Risks, health consequences, and response challenges for small-Island-based populations: observations from the 2017 Atlantic Hurricane Season. Disaster Med Public Health Prep 13:5–17

Solomon S, Qin D, Manning M, Alley R, Berntsen T, Bindoff N et al (2007) Technical summary. In: Solomon S, Qin D, Manning M, Chen Z, Marquis M, Averyt K, Tignor M, Miller H (eds) Climate change 2007: the physical science basis. Contribution of Working Group I to the fourth assessment report of the Intergovernmental Panel on Climate Change. Cambridge, United Kingdom and New York, NY, USA: Cambridge University Press

Sun YF, Chen CS, Beardsley RC, Xu QC, Qi JH, Lin HC (2013) Impact of current-wave interaction on storm surge simulation: a case study for Hurricane Bob. J Geophys Res Oceans 118:2685–2701

Tang HS, Qu K (2018) Potential Hydrodynamic Load on Coastal Bridges in the Greater New York Area due to Extreme Storm Surge and Wave, Final Report, University Transportation Research Center—Region 2. Performing Organization: City University of New York (CUNY)

Tang HS, Chien SI-Jy, Temimi M, Blain CA, Qu K, Zhao LH, Kraatz S (2013a) Vulnerability of population and transportation systems at east bank of Delaware Bay to coastal flooding in climate change conditions. Nat Hazards 69:141–163

Tang HS, Kraatz S, Wu XG, Cheng WL, Qu K, Polly J (2013b) Coupling of shallow water and circulation models for prediction of multiphysics coastal flows: method, implementation, and experiment. Ocean Eng 62:56–67

Tang HS, Kraatz S, Qu K, Chen GQ, Aboobaker N, Jiang CB (2014a) High-resolution survey of tidal energy towards power generation and influence of sea-level-rise: a case study at coast of New Jersey, USA. Renew Sustain Energy Rev 32:960–982

Tang HS, Qu K, Chen GQ, Kraatz S, Aboobaker N, Jiang CB (2014b) Potential sites for tidal power generation: a thorough search at coast of New Jersey, USA. Renew Sustain Energy Rev 39:412–425

Torres A, Lowden B, Ito K, Shuman S (2015) Lessons from hurricane sandy: analysis of vulnerabilities exposed by hurricane sandy and potential mitigation strategies in the northeastern united states. Prepared For: Dr. Richard B. Rood, Professor of AOSS 480. http://climateknowledge.org/figures/Rood_Climate_Change_AOSS480_Documents/AOSS480_2015_Sandy_Climate_Case_Study_Narrative.pdf

USGS CWD (2017) https://waterdata.usgs.gov/nwis/rt

Vecchi GA, Knutson T (2008) On estimates of historical north atlantic tropical cyclone activity. J Clim 21:3580–3600

Wienkea J, Oumeraci H (2005) Breaking wave impact force on a vertical and inclined slender pile—theoretical and large-scale model investigations. Coast Eng 52:435–462

Yin J, Schlesinger ME, Stouffer RJ (2009) Model projections of rapid sea-level rise on the northeast coast of the United States. Nat Geosci 2:262–266